

Implementation of the GRP scheme for computing radially symmetric compressible fluid flows

Jiequan Li^{a,*}, Tiegang Liu^b, Zhongfeng Sun^a

^a School of Mathematical Sciences, Capital Normal University, 100048 Beijing, PR China

^b LMIB and School of Mathematics and System Sciences, Beijing University of Aeronautics and Astronautics, 100830 Beijing, PR China

ARTICLE INFO

Article history:

Received 18 August 2008

Received in revised form 27 April 2009

Accepted 29 April 2009

Available online 18 May 2009

Keywords:

Radially symmetric fluid flows

The generalized Riemann problem (GRP) scheme

Numerical boundary condition

ABSTRACT

The study of radially symmetric compressible fluid flows is interesting both from the theoretical and numerical points of view. Spherical explosion and implosion in air, water and other media are well-known problems in application. Typical difficulties lie in the treatment of singularity in the geometrical source and the imposition of boundary conditions at the symmetric center, in addition to the resolution of classical discontinuities (shocks and contact discontinuities). In the present paper we present the implementation of direct generalized Riemann problem (GRP) scheme to resolve this issue. The scheme is obtained directly by the time integration of the fluid flows. Our new contribution is to show rigorously that the singularity is removable and derive the updating formulae for mass and energy at the center. Together with the vanishing of the momentum, we obtain new numerical boundary conditions at the center, which are then incorporated into the GRP scheme. The main ingredient is the passage from the Cartesian coordinates to the radially symmetric coordinates.

© 2009 Elsevier Inc. All rights reserved.

1. Introduction

The study of radially symmetric compressible fluid flows is classical [11], and theoretical and numerical considerations have been taken over past decades [28]. Spherical explosion and implosion in air, water and other media are typical examples [2]. Unlike one-dimensional case, spherical flow patterns are quite complex and new shocks can be born in unexpected regions [9,14]. Numerically speaking, we need to overcome the difficulty of geometrical singularity at the symmetric center and impose appropriate numerical boundary conditions, in addition to dealing with the resolution of classical discontinuities (shocks and contact discontinuities).

There were quite a few methods for the radially symmetric flows in the literature. In [3,12] the GRP method was used to track discontinuities. Their focus was not on the numerical treatment of the singularity at the center, but on the geometrical effect on numerical fluxes. In [30] the Glimm-type scheme was proposed, combined with operator splitting for the source term. Due to the inherent nature of Glimm scheme for hyperbolic conservation laws, it is at most first order. Furthermore, the operator splitting has well-known discrepancy in capturing steady state and in balancing flux gradient and the source. In [18] a practical method was devised by directly reducing the two-dimensional scheme in Cartesian coordinates to that in polar coordinates. In [23] the radially symmetric flows were studied by a modified Harten's TVD scheme. In most previous schemes, there were no systematic analysis of numerical boundary conditions and their imbedding into numerical schemes.

* Corresponding author. Address: School of Mathematical Sciences, Capital Normal University, North Load 105#, West Ring, 100048 Beijing, PR China. Tel.: +86 10 68905511; fax: +86 10 68900950.

E-mail addresses: jiequan@mail.cnu.edu.cn (J. Li), liutg@buaa.edu.cn (T. Liu), zfengsun@yahoo.com.cn (Z. Sun).

In this paper a particular concern is about numerical boundary conditions at the center $r = 0$ for the case of space dimension more than one. On one hand, no data is theoretically necessarily imposed on $r = 0$ because the presence of this boundary is totally caused by coordinate transformation. On the other hand, we require proper numerical boundary conditions in the implementation of the scheme although the vanishing velocity was often used through the symmetry argument in the literature. In addition, we need to overcome the singularity in the source of type $1/r$. Here we rigorously show that the singularity is removable at the center $r = 0$ and derive the updating formulae for mass and total energy. Together with the vanishing of momentum at the center, we obtain numerical boundary conditions, which are then incorporated into the GRP scheme. In this context, our main ingredient is to use the Jacobian factor from the Cartesian coordinates to the radially symmetric coordinates in order to remove the singularity factor $1/r$ in the source term. We point out that in the literature the velocity is often assumed to be zero at the center with the reflection boundary condition for (2.1) by the symmetry assumption. This treatment actually leads to the inconsistency with the governing Eq. (2.1), see Remark 3.3.

In the GRP scheme, the key point is how to solve the corresponding generalized Riemann problem at each grid point, which was originally achieved in [4] and subsequent works, e.g. [5,6]. The distinct feature of that original GRP scheme is the analytic resolution of curved rarefaction waves, and is based on the relevant Lagrangian scheme. In order to avoid the Lagrangian version and treat complicated sonic cases, we introduced Riemann invariants in [8,21] to resolve centered rarefaction waves (CRW). Thus the present scheme is directly Eulerian with easy extension to multi-dimensions and no special treatment is required for sonic cases. Indeed, this technique was already used for shallow water equations [20], compressible fluid flows [8] and more general systems [7]. The further advantage of this approach is that the source term (geometrical) effect is included in numerical fluxes. This can be seen from the following simple scalar equation:

$$\frac{\partial u}{\partial t} = -\frac{\partial f(u)}{\partial r} + s(r, u), \quad (1.1)$$

where the time derivative is replaced by the spatial derivative plus the source term via the Lax–Wendroff approach. Then this fact is built into the numerical fluxes as an important ingredient in the GRP scheme. Just at this point, we always have second order accuracy in time even though the initial data is given to be piecewise constant (first order in space), see Remark 4.2. The discretization of source term is realized with the mid-point rule in time and the trapezoidal rule in space in order to balance the variation of fluxes well, which is an important factor to devise a well-balanced scheme, see Remark 2.3.

The purpose of this work is to extend the GRP scheme to solve the radially symmetric flows and the resulting scheme is different from [3,12,22]. We pay our special attention to the treatment of the geometrical singularity at the center and the numerical boundary conditions. We point out in passing that our approach can also be applied to duct flows of variable cross-section. In addition, we often use acoustic approximation in the GRP scheme when the state changes small at a grid point. To show the performance of the current method, we apply it to the Noh problem of spherically converging flows, the Sedov–Taylor strong point explosion problem, explosion and implosion problems. The Noh problem and the Sedov–Taylor problem have exact solutions [6,25,29] so that there are explicit illustrations about the performance of the present scheme. The analysis and simulations of explosion and implosion problems can be found in [27,24,26,9,10,13,18,23,30] and references therein. We can compare to show our results are competitive.

We organize this paper as follows. In Section 2 we summarize our generalized Riemann problem (GRP) scheme. The numerical boundary conditions at $r = 0$ are rigorously derived in Section 3. The generalized Riemann problem at each grid point is resolved in Section 4 for the spherical flows. The useful acoustic approximation is given in Section 5. We simulate the Noh problem, the Sedov–Taylor problem, the explosion and implosion problems, as typical examples, to validate the present scheme in Section 6. To make the present paper self-contained, we put some detailed derivation of the GRP scheme and useful notations in Appendices.

2. Implementation of the GRP scheme

The equations of radially symmetric compressible fluid flows can be written in the form,

$$\frac{\partial U}{\partial t} + \frac{\partial F(U)}{\partial r} = \Psi(r, U), \quad (2.1)$$

$$U = \begin{pmatrix} \rho \\ \rho u \\ \rho E \end{pmatrix}, \quad F(U) = \begin{pmatrix} \rho u \\ \rho u^2 + p \\ u(\rho E + p) \end{pmatrix}, \quad \Psi(r, U) = -\frac{m-1}{r} \begin{pmatrix} \rho u \\ \rho u^2 \\ u(\rho E + p) \end{pmatrix},$$

where $E = e + \frac{u^2}{2}$. ρ, u, e are density, radial velocity and internal energy, respectively, and $p = p(\rho, e)$ is the pressure, $r \geq 0$ is the radius. The integer m represents the spatial dimension number. As $m = 1, 2, 3$, (2.1) describes planar, cylindrical and spherical flows, respectively. The source term $\Psi(r, U)$ is geometrical and results from the transformation from the Cartesian coordinates to the radially symmetric coordinates.

Remark 2.1. System (2.1) can also be expressed as

$$\frac{\partial r^{m-1}U}{\partial t} + \frac{\partial r^{m-1}F(U)}{\partial r} = \tilde{\Psi}(r, U), \quad \tilde{\Psi}(r, U) = (m-1)r^{m-2}(0, p, 0)^T. \quad (2.2)$$

This form illustrates the conservation of mass and energy clearly, as well as the influence of geometry on the momentum. In the GRP scheme, we prefer to use (2.1) since all computations are performed for the primitive variables.

We propose to develop a high resolution numerical scheme for (2.1) by the analytic time integration. The scheme is implemented with the main ingredient of the resolution of the generalized Riemann problem (GRP) for (2.1) at each grid point $r_{j+1/2} = (j + \varepsilon)\Delta r$, $j \geq 0$, subject to the piecewise linear data

$$U(r, t_n) = U_j^n + \sigma_j^n(r - r_j), \quad r \in (r_{j-1/2}, r_{j+1/2}), \quad j = 0, 1, \dots, K, \quad (2.3)$$

where we divide a computational domain $[0, M]$ into $K + 1$ cells $C_j = (r_{j-1/2}, r_{j+1/2})$, $r_j = \frac{1}{2}(r_{j-1/2} + r_{j+1/2})$, $0 \leq j \leq K$, and set $r_{-1/2} = 0$, the small parameter $0 < \varepsilon \leq 1$ being introduced numerically in order to deal with the singularity at the center $r = 0$. Thus the cell $C_0 = [0, \varepsilon\Delta r]$ represents the left boundary cell at the center $r = 0$ and the cell $C_K = [r_{K-1/2}, r_{K+1/2}]$ is the right boundary cell. In practice, we choose $\varepsilon = 1$. The vector σ_j^n is the constant slope of $U(r, t_n)$ over cell C_j at time $t_n = n\Delta t$, $j \in \{0\} \cup \mathbb{Z}^+$, $n \in \mathbb{Z}^+$, Δr is the length of the cell C_j ($j > 1$) and Δt the size of time step. Within the accuracy of second order, we use mid-point values

$$U_{j+1/2}^{n+1/2} = U(r_{j+1/2}, (n + 1/2)\Delta t), \quad j = 0, 1, \dots, K - 1, \quad (2.4)$$

to incorporate into numerical fluxes and the discretization of the source term. Here we summarize the major steps of the GRP method, as in [4,8], in the following:

Step 1. Given piecewise linear initial data (2.3), we calculate mid-point values $U_{j+1/2}^{n+1/2}$ approximately,

$$U_{j+1/2}^{n+1/2} = U_{j+1/2}^n + \frac{\Delta t}{2} \left(\frac{\partial U}{\partial t} \right)_{j+1/2}^n, \quad j = 0, 1, \dots, K - 1, \quad (2.5)$$

where $(\partial U / \partial t)_{j+1/2}^n$ will be given in Section 4 and particularly in Section 5 for acoustic approximation. The notation $U_{j+1/2}^n = U^A(r_{j+1/2}, t_n + 0)$ and $U^A(r, t)$ is the local solution at $(r_{j+1/2}, t_n)$ to the following Riemann problem:

$$\begin{aligned} \frac{\partial U}{\partial t} + \frac{\partial F(U)}{\partial r} &= 0, \quad r > 0, \quad t > t_n, \\ U(r, t_n) &= \begin{cases} U_L := U_j^n + (r_{j+1/2} - r_j)\sigma_j^n, & r < r_{j+1/2}, \\ U_R := U_{j+1}^n + (r_{j+1/2} - r_{j+1})\sigma_{j+1}^n, & r > r_{j+1/2}. \end{cases} \end{aligned} \quad (2.6)$$

which can be solved by an exact or approximate Riemann solver [32].

Step 2. Evaluate the interior cell averages U_j^{n+1} , $j = 1, \dots, K - 1$, by using the updating formula

$$U_j^{n+1} = U_j^n - \frac{\Delta t}{\Delta r} (F(U_{j+1/2}^{n+1/2}) - F(U_{j-1/2}^{n+1/2})) + \frac{\Delta t}{2} (\Psi(r_{j+1/2}, U_{j+1/2}^{n+1/2}) + \Psi(r_{j-1/2}, U_{j-1/2}^{n+1/2})). \quad (2.7)$$

The source term $\Psi(r, U)$ is discretized with the mid-point rule in time and the trapezoidal rule in space. For the boundary value U_0^{n+1} , we have $(\rho u)_0^{n+1} = 0$, and

$$\rho_0^{n+1} = \rho_0^n - m \cdot \frac{\Delta t}{\varepsilon \Delta r} (\rho u)_{1/2}^{n+1/2}, \quad (\rho E)_0^{n+1} = (\rho E)_0^n - m \cdot \frac{\Delta t}{\varepsilon \Delta r} (u(\rho E + p))_{1/2}^{n+1/2}. \quad (2.8)$$

These will be given in Section 3. We use the transmission boundary condition at the right boundary [15].

Step 3. Update the slope σ_j^{n+1} by the following procedure. Define:

$$U_{j+1/2}^{n+1,-} = U_{j+1/2}^n + \Delta t \left(\frac{\partial U}{\partial t} \right)_{j+1/2}^n, \quad j = 0, 1, \dots, K - 1, \quad \sigma_j^{n+1,-} = \frac{1}{\Delta r} (\Delta U)_j^{n+1,-} := \frac{1}{\Delta r} (U_{j+1/2}^{n+1,-} - U_{j-1/2}^{n+1,-}), \quad j = 1, \dots, K - 1. \quad (2.9)$$

In order to suppress local oscillations near discontinuities, we apply to $\sigma_j^{n+1,-}$ a monotonicity algorithm-slope limiter,

$$\begin{aligned} \sigma_j^{n+1} &= \minmod \left(\alpha \frac{U_j^{n+1} - U_{j-1}^{n+1}}{\Delta r}, \sigma_j^{n+1,-}, \alpha \frac{U_{j+1}^{n+1} - U_j^{n+1}}{\Delta r} \right), \quad j = 2, \dots, K - 1, \\ \sigma_1^{n+1} &= \minmod \left(\alpha \frac{U_1^{n+1} - U_0^{n+1}}{(\varepsilon + 1)\Delta r/2}, \sigma_1^{n+1,-}, \alpha \frac{U_2^{n+1} - U_1^{n+1}}{\Delta r} \right), \quad \sigma_0^{n+1} = \minmod \left(\frac{U_{1/2}^{n+1,-} - U_0^{n+1}}{\varepsilon \Delta r/2}, \sigma_1^{n+1} \right), \\ \sigma_K^{n+1} &= \minmod \left(\frac{U_{K-1/2}^{n+1,-} - U_{K-1}^{n+1}}{\Delta r/2}, \sigma_{K-1}^{n+1} \right), \end{aligned} \quad (2.10)$$

where the parameter $\alpha \in [0, 2)$. This monotonicity algorithm corresponds a non-sawtooth case for $\alpha \in [0, 1]$ and a sawtooth case for $\alpha \in (0, 2)$. In our scheme, α is taken in $[1.5, 2)$. The minmod function can be found in [4,15].

Remark 2.2. As $r_{j+1/2}$ is close to zero ($j \geq 0$), there is a singularity factor $1/r_{j+1/2}$ in Ψ . This does not cause any problem. In fact, Δr and Δt coexist so that $\Delta t/\Delta r$ is bounded, which is implied by the standard CFL condition.

Remark 2.3. In (2.7) we use the (mid-point) values $U_{j+1/2}^{n+1/2}$ in the discretization of source term Ψ . Note that these values are already computed for numerical fluxes without extra manipulation. In addition such discretization can keep second order accuracy both in space and time (trapezoidal rule in space and mid-point rule in time), and to well balance the variation of fluxes.

Remark 2.4. The key part of the GRP scheme is the calculation of $(\partial U/\partial t)_{j+1/2}^n$, which is obtained by solving (4.4) and (4.7), to be presented in Section 4. When the acoustic approximation is applied, we go to Section 5. All coefficients can be consulted in Appendix E. Therefore, in the practical implementation of the GRP scheme, we just need to use this framework and consult the coefficients in Appendix E and leave the other parts for the mathematical interest.

3. The boundary condition at the center

As noted in many literatures [1,23,30], there are two major difficulties near the center $r = 0$: Numerical boundary conditions and the singular nature proportional to $1/r$. The latter is relatively simple and it can be settled down with the CFL restriction. The former is an inherent problem in the scheme.

We will first show a local compatibility relation between the space variation and the time evolution of conservative variables at the center. The vanishing of velocity (equivalently the momentum) can be obtained simply through the symmetry argument [1,6,14,23]. This relation will further provide the consistency of the numerical boundary conditions in Proposition 3.2 with the governing systems (2.1).

Proposition 3.1. *At the center $r = 0$, the velocity must vanish, i.e. $u(0, t) \equiv 0$, and the derivatives of mass and energy satisfy*

$$\left(\frac{\partial \rho}{\partial t}\right)_0 + m \left(\frac{\partial(\rho u)}{\partial r}\right)_0 = 0, \quad \left(\frac{\partial(\rho E)}{\partial t}\right)_0 + m \left(\frac{\partial(\rho E + p)u}{\partial r}\right)_0 = 0, \quad (3.1)$$

provided that the flow is smooth, where the subscript 0 stands for the flow state at the center.

Proof. The integral mass conservative laws for a fixed domain Ω can be written as follows:

$$\frac{\partial}{\partial t} \int_{\Omega} \rho dV + \int_{\partial\Omega} \rho \vec{v} \cdot \vec{n} dS = 0, \quad (3.2)$$

where \vec{v} is the velocity vector, \vec{n} is the outward normal unit vector pertaining to the domain boundary $\partial\Omega$.

(I) *Spherically symmetric flow ($m = 3$):* For the spherically symmetric flow, Ω is taken as a sphere of radius Δr centered at the origin. With the spherical coordinate transformation, (3.2) can be rewritten as

$$\int_0^{2\pi} d\phi \int_0^{\pi} \sin \theta d\theta \int_0^{\Delta r} r^2 \frac{\partial \rho}{\partial t} dr + (\Delta r)^2 \rho u(\Delta r, t) \int_0^{2\pi} d\phi \int_0^{\pi} \sin \theta d\theta = 0. \quad (3.3)$$

Using the mean value theorem of integration, (3.3) can be reduced to

$$\frac{\partial \rho(\xi \Delta r, t)}{\partial t} + 3 \frac{\rho u(\Delta r, t)}{\Delta r} = 0, \quad (3.4)$$

where $0 \leq \xi \leq 1$. With the symmetry argument, we conclude the velocity (or momentum) vanishes at the center, i.e. $u(0, t) = 0$. Therefore, (3.4) immediately implies the first identity of (3.1). Similarly, we obtain the second identity.

(II) *Cylindrically symmetric flow ($m = 2$):* In a similar way, we can show that Proposition 3.1 holds for the cylindrically symmetric flow, for which Ω is now taken to be a small cylinder of radius Δr and any height Δz centered at the origin. \square

We are now at the position to find numerical boundary data at $r = 0$, which is the main contribution in the present paper. The result is stated in the following proposition.

Proposition 3.2. *The numerical boundary condition $U_0^{n+1} = (\rho_0^{n+1}, (\rho u)_0^{n+1}, (\rho E)_0^{n+1})^T$ at the center $r = 0$ can be expressed as follows:*

$$\rho_0^{n+1} = \rho_0^n - m \cdot \frac{\Delta t}{\varepsilon \Delta r} (\rho u)_{1/2}^{n+1/2}, \quad (\rho u)_0^{n+1} = 0, \quad (\rho E)_0^{n+1} = (\rho E)_0^n - m \cdot \frac{\Delta t}{\varepsilon \Delta r} (u(\rho E + p))_{1/2}^{n+1/2}, \quad (3.5)$$

where the mid-point value $U_{1/2}^{n+1/2}$ can be obtained by (2.5) and $0 < \varepsilon \ll 1$ is a constant.

Proof. From Proposition 3.1, we know that $u(0, t) \equiv 0$. Then we consider the momentum average over the cell $[0, \varepsilon \Delta r]$,

$$(\rho u)_0 := \frac{1}{\varepsilon \Delta r} \int_0^{\varepsilon \Delta r} \rho u(r, t) dr. \quad (3.6)$$

As ε is sufficient small, we have approximately

$$(\rho u)_0 = \frac{1}{\varepsilon \Delta r} \int_0^{\varepsilon \Delta r} \rho u(r, t) dr \rightarrow \rho u(0, t) = 0. \quad (3.7)$$

This is compatible with $\rho u(0, t) \equiv 0$ as $\varepsilon \rightarrow 0$. Thus we take $(\rho u)_0^{n+1} = 0$ as the constant ε is small.

For the evolution of mass and energy, we use the finite volume formulation of (2.1) over the control volume $[0, \varepsilon \Delta r] \times [t_n, t_{n+1}]$ with a multiplication factor r^{m-1} , $m > 1$,

$$\int_{t_n}^{t_{n+1}} \int_0^{\varepsilon \Delta r} r^{m-1} \frac{\partial U}{\partial t} dr dt + \int_{t_n}^{t_{n+1}} \int_0^{\varepsilon \Delta r} r^{m-1} \frac{\partial F(U)}{\partial r} dr dt = \int_{t_n}^{t_{n+1}} \int_0^{\varepsilon \Delta r} r^{m-1} \Psi(r, U) dr dt, \quad (3.8)$$

where the factor r^{m-1} plays an important role of the Jacobian in the transformation from the Cartesian coordinates to the spherical coordinates. When this idea is used, both the singularity at $r = 0$ can be removed and the source term can be effectively treated.

With the simple technique of numerical integration, we obtain formally

$$\int_{t_n}^{t_{n+1}} \int_0^{\varepsilon \Delta r} r^{m-1} \frac{\partial U}{\partial t} dr dt = \frac{(\varepsilon \Delta r)^m}{m} \cdot (U_0^{n+1} - U_0^n) + O((\Delta r)^{m+2}), \quad (3.9)$$

where U_0^n is the average value of $U(r, t_n)$ over the cell $[0, \varepsilon \Delta r]$,

$$U_0^n = \frac{1}{\varepsilon \Delta r} \int_0^{\varepsilon \Delta r} U(r, t_n) dr. \quad (3.10)$$

We take the integration by parts for the second term in the left hand side of (3.8) to obtain

$$\begin{aligned} \int_{t_n}^{t_{n+1}} \int_0^{\varepsilon \Delta r} r^{m-1} \frac{\partial F(U)}{\partial r} dr dt &= \int_{t_n}^{t_{n+1}} r^{m-1} F(U(\cdot, t))|_0^{\varepsilon \Delta r} dt - \int_{t_n}^{t_{n+1}} \int_0^{\varepsilon \Delta r} (m-1) r^{m-2} F(U) dr dt \\ &= (\varepsilon \Delta r)^{m-1} \int_{t_n}^{t_{n+1}} F(U(\varepsilon \Delta r, t)) dt - (m-1) \int_{t_n}^{t_{n+1}} \int_0^{\varepsilon \Delta r} r^{m-2} F(U) dr dt. \end{aligned} \quad (3.11)$$

When the mass and energy equations of (2.1) are considered separately, we obtain by incorporating (3.8) and (3.9),

$$\rho_0^{n+1} = \rho_0^n - \frac{m}{\varepsilon \Delta r} \int_{t_n}^{t_{n+1}} \rho u(\varepsilon \Delta r, t) dt, \quad (\rho E)_0^{n+1} = (\rho E)_0^n - \frac{m}{\varepsilon \Delta r} \int_{t_n}^{t_{n+1}} u(\rho E + p)(\varepsilon \Delta r, t) dt. \quad (3.12)$$

Then we use the mid-point rule to evaluate the single time integrals and obtain (3.5) within second order accuracy. \square

Remark 3.3. In the literature, a reflection boundary condition is often adopted at the center for (2.1) directly, the velocity is assumed to be zero and the (geometrical) source does not take effect. Then the updating formulae at the first cell C_0 become (3.1) with $m = 1$. This leads to the inconsistency with the governing Eq. (2.1).

Remark 3.4. Here we provide the updating formulae for the density and energy (3.5), which are compatible with (3.1). Certainly, (3.5) can also be derived from (2.2) with almost the same argument. We should notice that all above arguments are based on the smooth assumption, which is not always realistic, for example, mainly at the collision of shocks. Nevertheless, these boundary conditions are shown to be effective when applied to the examples in Section 6.

4. The resolution of the generalized Riemann problem

In order to derive the GRP scheme, we need to solve the generalized Riemann problem for (2.1) at each grid point $(r, t) = (r_{j+1/2}, t_n)$, $j = 0, \dots, K-1$. For convenience, we set the cell interface, as in the usual setting of the generalized Riemann problem, as $(r_0, 0) := (r_{j+1/2}, t_n)$, $r_0 > 0$, and assume the piecewise linear data as

$$U(r, 0) = \begin{cases} U_L + (r - r_0)U'_L, & r < r_0, \\ U_R + (r - r_0)U'_R, & r > r_0, \end{cases} \quad (4.1)$$

where U_L, U_R, U'_L and U'_R are constant vectors,

$$U_L = U_j^n + (r_{j+1/2} - r_j)\sigma_j^n, \quad U_R = U_{j+1}^n + (r_{j+1/2} - r_{j+1})\sigma_{j+1}^n, \quad U'_L = \sigma_j^n, \quad U'_R = \sigma_{j+1}^n, \quad (4.2)$$

and they can be found in (2.6). Then the solution $U(r, t)$ of (2.1) and (4.1) is smooth at least for a short time along the interface $r = r_0$. Denote

$$U_* = U(r_0, 0^+) = \lim_{t \rightarrow 0^+} U(r_0, t), \quad \left(\frac{\partial U}{\partial t} \right)_* = \frac{\partial U}{\partial t}(r_0, 0^+) = \lim_{t \rightarrow 0^+} \frac{\partial U}{\partial t}(r_0, t). \quad (4.3)$$

The value U_* is nothing but the limiting value at $t = 0$ of the Riemann solution $U^A(r, t)$ along $r = r_0$, which is obtained by solving the Riemann problem (2.6). This solution $U^A(r, t)$ determines the local structure of $U(r, t)$ at $r = r_0$, see [19]. Hence we are left with the calculation of $(\partial U / \partial t)_*$.

The instantaneous value $(\partial U / \partial t)_*$ is calculated depending on local wave configurations. If the t -axis is located inside the intermediate region (a wave propagates to the left and a wave to the right), we need to solve a linear system of two-equations. Otherwise, the value is just taken upwind.

Proposition 4.1 (Nonsonic case). Assume that the t -axis is located in the intermediate region. Then the limiting values $(\partial p / \partial t)_*$ and $(\partial u / \partial t)_*$ satisfy the linear relations

$$h_L \left(\frac{\partial u}{\partial t} \right)_* + q_L \left(\frac{\partial p}{\partial t} \right)_* = k_L, \quad h_R \left(\frac{\partial u}{\partial t} \right)_* + q_R \left(\frac{\partial p}{\partial t} \right)_* = k_R, \quad (4.4)$$

where h_L, h_R, q_L, q_R, k_L and k_R are summarized for all cases in Appendix E, respectively. These parameters depend only on the initial data (4.1) and the local Riemann solution $R^A(0; U_L, U_R)$.

Remark 4.2. Note that if $U'_L = U'_R = 0$, the GRP scheme has only first order accuracy in space. However, since the geometrical source term is present, the terms k_L and k_R do not vanish and so this scheme still has second order accuracy in time and includes the source term effect in the numerical fluxes. Certainly, it is reduced to the first order Godunov scheme [16] if the source term is absent (one-dimensional case).

Remark 4.3. Note that k_L and k_R include the factor of type $1/r$ (cf. (E.1)). If $r_0 \sim \Delta r \rightarrow 0$, we need special treatment. In practice, we propose to obtain the value $\Delta t \cdot \frac{\partial U}{\partial t}$ at $(r_0, 0)$ instead of $\frac{\partial U}{\partial t}$. Hence we multiply (4.4) by Δt to obtain,

$$h_L \cdot \Delta t \left(\frac{\partial u}{\partial t} \right)_* + q_L \cdot \Delta t \left(\frac{\partial p}{\partial t} \right)_* = k_L \Delta t, \quad h_R \cdot \Delta t \left(\frac{\partial u}{\partial t} \right)_* + q_R \cdot \Delta t \left(\frac{\partial p}{\partial t} \right)_* = k_R \Delta t. \quad (4.5)$$

Using the fact that $\Delta t \sim \Delta r \sim r_0$ by the CFL condition, the singularity caused by $1/r_0$ can be removed. Thus we replace (4.4) by (4.5) to obtain a new linear algebraic equations. In other parts, we can take the same approach if r_0 is very small.

When the t -axis ($r = r_0$) is located inside a rarefaction fan, we have a sonic case. Since one of the characteristic curves becomes tangential to the t -axis, the situation becomes much simpler. Indeed, we have the following Proposition.

Proposition 4.4 (Sonic case). Assume that the t -axis is located inside the rarefaction wave associated with the $u - c$ characteristic family. Then we have

$$\left(\frac{\partial u}{\partial t} \right)_* = d_L + \frac{m-1}{r_0} u_*^2, \quad \left(\frac{\partial p}{\partial t} \right)_* = \rho_* u_* d_L, \quad (4.6)$$

where d_L is given in (E.3), and $c_{1*} = u_*$ in (E.3).

Remark 4.5. The approach to prove Proposition 4.4 can be found in the proof of Theorem 5.4 in [8, p. 30].

Now it remains to calculate $(\partial \rho / \partial t)_*$. This calculation depends on whether the contact discontinuity propagates to the left or the right. To be more precise, we calculate $(\partial \rho / \partial t)_*$ from the left-hand side if $u_* > 0$; and in the right-hand side if $u_* < 0$.

Proposition 4.6. The computation of $(\partial \rho / \partial t)_*$. The limiting value $(\partial \rho / \partial t)_*$ is calculated as follows, depending on the propagation of contact discontinuity:

$$g_\rho \left(\frac{\partial \rho}{\partial t} \right)_* + g_p \left(\frac{\partial p}{\partial t} \right)_* + g_u \left(\frac{\partial u}{\partial t} \right)_* = f, \quad (4.7)$$

where g_ρ, g_p, g_u and f are constant, depending on the initial data (4.1) and the associated Riemann solution $R^A(0; U_L, U_R)$. They are expressed in Appendix E.

Remark 4.7. When all the waves move to right, as shown in Fig. 4.1, the region I is smooth. The limiting values $(\partial U / \partial t)_*$ are derived from the system (2.1) directly,

$$\left(\frac{\partial \rho}{\partial t} \right)_* = - \left(\rho_L u'_L + u_L \rho'_L + \frac{m-1}{r_0} \rho_L u_L \right), \quad \left(\frac{\partial p}{\partial t} \right)_* = - \left(u_L p'_L + \gamma p_L u'_L + \frac{m-1}{r_0} \gamma p_L u_L \right), \quad \left(\frac{\partial u}{\partial t} \right)_* = - (p'_L / \rho_L + u_L u'_L), \quad (4.8)$$

where U_L, U'_L are given in (4.2). When all the waves move to left, we can calculate $(\partial U / \partial t)_*$ from the right hand, as a result, we just need to replace U_L, U'_L in (4.8) by U_R, U'_R .

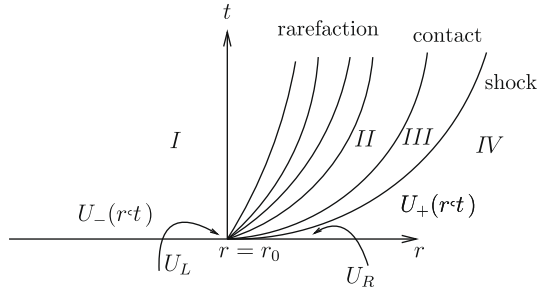


Fig. 4.1. Wave pattern for the GRP. The initial data $U_0(r) = U_L + (r - r_0)U'_L$ for $r < r_0$ and $U_0(r) = U_R + (r - r_0)U'_R$ for $r > r_0$.

5. Acoustic case

As $|U_L - U_R| \ll 1$, we will use the acoustic approximation. Let us look at the initial data $U(r, 0)$ in (4.1) satisfying $U_L = U_R$ and $U'_L \neq U'_R$. Then the solution to the associated Riemann problem is constant $U_* = U^A(r_0, 0) \equiv U_L = U_R$ and only linear waves emanate from the point $(r_0, 0)$. Denote $V = U - U_*$. Then we can linearize (2.1) around $U = U_*$ to obtain

$$\frac{\partial V}{\partial t} + DF(U_*) \frac{\partial V}{\partial r} = \Psi(r_0, U_*). \quad (5.1)$$

Diagonalize the system (5.1) to obtain

$$\frac{\partial W}{\partial t} + \Lambda(W_*) \frac{\partial W}{\partial r} = L(U_*) \Psi(r_0, U_*), \quad (5.2)$$

where $W = L(U_*)V$, $L = (L_1, L_2, L_3)$, L_i is the left (row) eigenvector associated with the eigenvalue λ_i of $DF(U_*)$, $i = 1, 2, 3$, $\lambda_1 = u_* - c_*$, $\lambda_2 = u_*$ and $\lambda_3 = u_* + c_*$, and Λ is a diagonal matrix with entries $\lambda_i(U_*)$. Therefore we can calculate the time derivative of W , as in the scalar case,

$$\left(\frac{\partial W}{\partial t} \right)_* = \lim_{t \rightarrow 0^+} \frac{\partial W}{\partial t}(r_0, t) = - \left[\frac{|A| + A}{2} W'_L + \frac{|A| - A}{2} W'_R \right] + L(U_*) \Psi(r_0, U_*), \quad (5.3)$$

where $|A| = \text{diag}(|\lambda_1|, |\lambda_2|, |\lambda_3|)$. Returning to the primitive variables U we obtain

$$\left(\frac{\partial U}{\partial t} \right)_* = \left(\frac{\partial V}{\partial t} \right)_* = L^{-1}(U_*) \left(\frac{\partial W}{\partial t} \right)_*. \quad (5.4)$$

Proposition 5.1 (Acoustic case). When $U_L = U_* = U_R$ and $U'_L \neq U'_R$, we have the acoustic case. If $u_* - c_* < 0$ and $u_* + c_* > 0$, then $(\partial u / \partial t)_*$ and $(\partial p / \partial t)_*$ can be solved to be

$$\begin{aligned} \left(\frac{\partial u}{\partial t} \right)_* &= -\frac{1}{2} \left[(u_* + c_*) \left(u'_L + \frac{p'_L}{\rho_* c_*} \right) + (u_* - c_*) \left(u'_R - \frac{p'_R}{\rho_* c_*} \right) \right], \\ \left(\frac{\partial p}{\partial t} \right)_* &= -\frac{\rho_* c_*}{2} \left[(u_* + c_*) \left(u'_L + \frac{p'_L}{\rho_* c_*} \right) - (u_* - c_*) \left(u'_R - \frac{p'_R}{\rho_* c_*} \right) \right] - \frac{m-1}{r_0} \rho_* u_* c_*^2. \end{aligned} \quad (5.5)$$

Then the quantity $(\partial \rho / \partial t)_*$ is calculated from the equation of state $p = p(\rho, S)$,

$$\left(\frac{\partial \rho}{\partial t} \right)_* = \begin{cases} \frac{1}{c_*^2} \left[\left(\frac{\partial p}{\partial t} \right)_* + u_* (p'_L - c_*^2 \rho'_L) \right] & \text{if } u_* = u_L = u_R > 0, \\ \frac{1}{c_*^2} \left[\left(\frac{\partial p}{\partial t} \right)_* + u_* (p'_R - c_*^2 \rho'_R) \right], & \text{if } u_* = u_L = u_R < 0. \end{cases} \quad (5.6)$$

Remark 5.2. We can take the limit $U_L = U_* = U_R$ for the results in Propositions 4.1 and 4.6 to yield Proposition 5.1.

6. Numerical examples

In this section we display several typical examples. One purpose is to illustrate the performance of our scheme. The other is to show the rich wave patterns in the explosion and implosion problems. In the following numerical examples, $\gamma > 1$ is the adiabatic index and α, ε are parameters in (2.10) and (3.5), respectively. The Courant number μ is defined as

$$\mu_{\text{CFL}} = \frac{\Delta t}{\varepsilon \Delta r} \max_{j=0,1,\dots,K} (|u_j^n| + c_j^n).$$

We take $\mu_{\text{CFL}} = 0.4$. The parameter ε is best chosen to be 1.0, in the examples. The effect of various choice of the parameter ε is analyzed through the L^1 -error. Besides, for the further verification of the present scheme, we compare the GRP results with the corresponding exact solutions or those by the modified Harten's TVD scheme [23].

6.1. Noh problem

Our first example is the spherically converging flow of a cold (zero-pressure) perfect gas with $\gamma = 5/3$, having the uniform initial conditions

$$[\rho, u, p] = [1, -1, 0], \quad 0 < r \leq 100,$$

which has been proposed by Noh [25] as a test case having an exact (self-similar) solution, see also [24,26] for some recent simulations. The solution consists of an expanding spherical shock (starting from the center at $t = 0$). The fluid behind the shock is quiescent with uniform pressure p and density ρ . We set initial pressure to be 10^{-6} instead of zero pressure. We take the boundary value over the right cell C_K ,

$$[\rho, u, p]^{n+1}(r) = [(1 + t_{n+1}/r)^2, -1, 10^{-6}], \quad r \in C_K = [r_{K-1/2}, r_{K+1/2}],$$

which is the exact solution at $t = t_{n+1}$. Results of the Noh problem are shown in Fig. 6.1. The agreement with the exact solution is very good, discrepancies occurring primarily for the density distribution near the center. As explained in [6], this error is due to the “startup” of the captured shock near the center, where the numerical dissipation generates an entropy higher than the exact value. These discrepancies can be weakened by using the exact value of solution as the boundary data at the center [3], which is actually impractical. We can see that our scheme produces a good result in Fig. 6.1 by comparing with those in [24,26].

Furthermore, we show the relation between L^1 -error and the parameter ε in Fig. 6.2. The relative L^1 -error is defined as $\|u - U\|_1 = \sum_i |u_i - U_i| \Delta r_i / \sum_i |u_i| \Delta r_i$, where u_i, U_i are the exact and numerical solutions, respectively. The L^1 -error becomes very large as $\varepsilon < 0.2$. Hence we just compute L^1 -error when $\varepsilon \geq 0.2$.

In the following numerical examples, we take $\gamma = 1.4$.

6.2. The Sedov–Taylor blast wave problem

In our second example, we choose the Sedov–Taylor blast wave problem to simulate strong shock propagation. Numerical difficulties lie in the low density and the high temperature near the center. The analytical solution is given by Sedov [29]

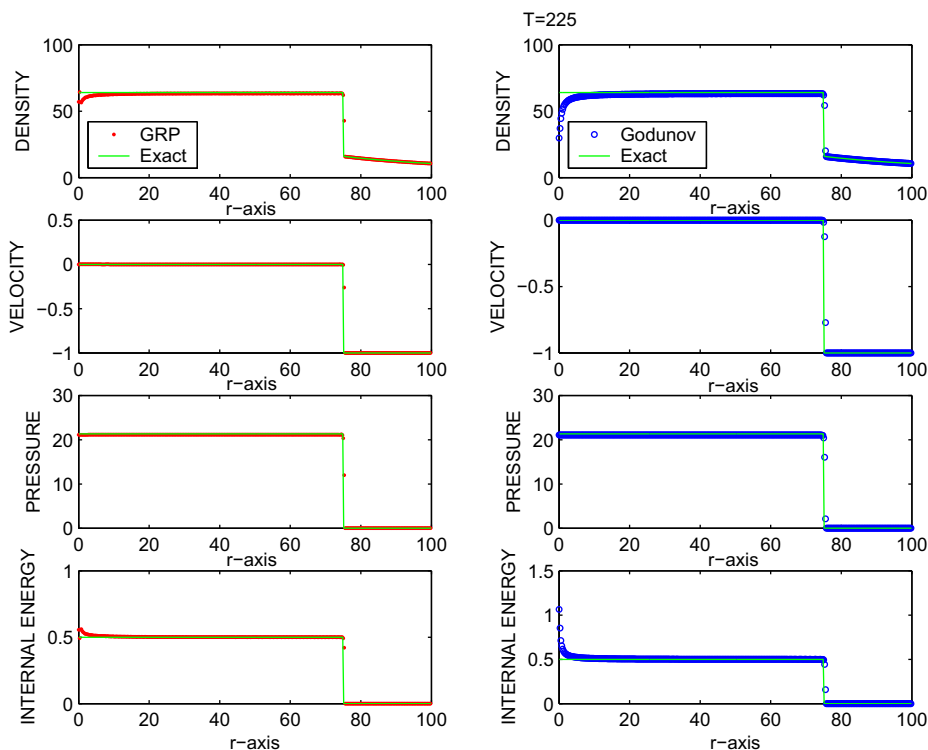


Fig. 6.1. Numerical results for Noh problem: 400 grids are used, $\alpha = 1.5$. Left column is the GRP solution; and the right-column is the Godunov solution.

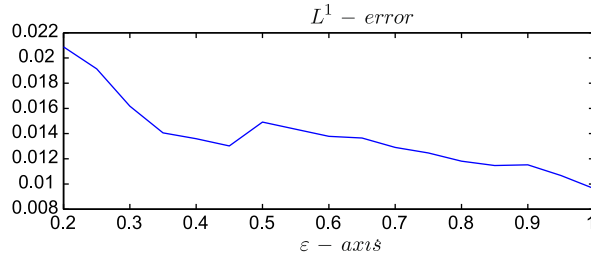


Fig. 6.2. L^1 -error estimate for the Noh problem at $T = 225$.

under the assumption that the atmospheric pressure relative to the pressure inside the explosion is negligible. The gas is initially at rest with $\rho = 1.0, p = 1.08 \times 10^5$ for $0 \leq r \leq 1/500$ and $\rho = 1.0, p = 10^{-6}$ for $1/500 < r \leq 1$. Results at $T = 0.08$ are shown in Fig. 6.3. We observe that the density is close to zero nearby the explosion center and the temperature is very high. The GRP scheme does it quite well, compared to the Godunov scheme, even to those in [27,24,26].

The L^1 -error is shown in Fig. 6.4 in terms of the parameter ε . In analogy with the first example, $\varepsilon = 1$ is the best choice in practice.

6.3. The numerical simulation of spherical explosion in air

For the spherical explosion case, we use the test model that has been analyzed by Brode [10], investigated experimentally in [9] and simulated in [23]. The gas is initially at rest with $\rho = 21.7333, p = 15.514$ for $0 \leq r \leq 5$ and $\rho = 2.0, p = 1.0$ for $5 < r \leq 50$. These data are non-dimensional. The physics for the spherical explosion is quite complex. Besides an inward rarefaction wave in the high-pressure region, an outward shock wave in the low-pressure region and a contact discontinuity between the rarefaction wave and the shock wave, there is a second shock subsequently arising at the tail of the rarefaction wave as shown by both previous experiments [9,14] and numerical simulations [31,23]. The generation mechanism of the second shock has been analyzed in length in a previous work [23], the shock is outward-facing before $T = 9.5$ and becomes inward-facing subsequently. Because the second shock wave forms in the expanding wave region, it is rather weak initially

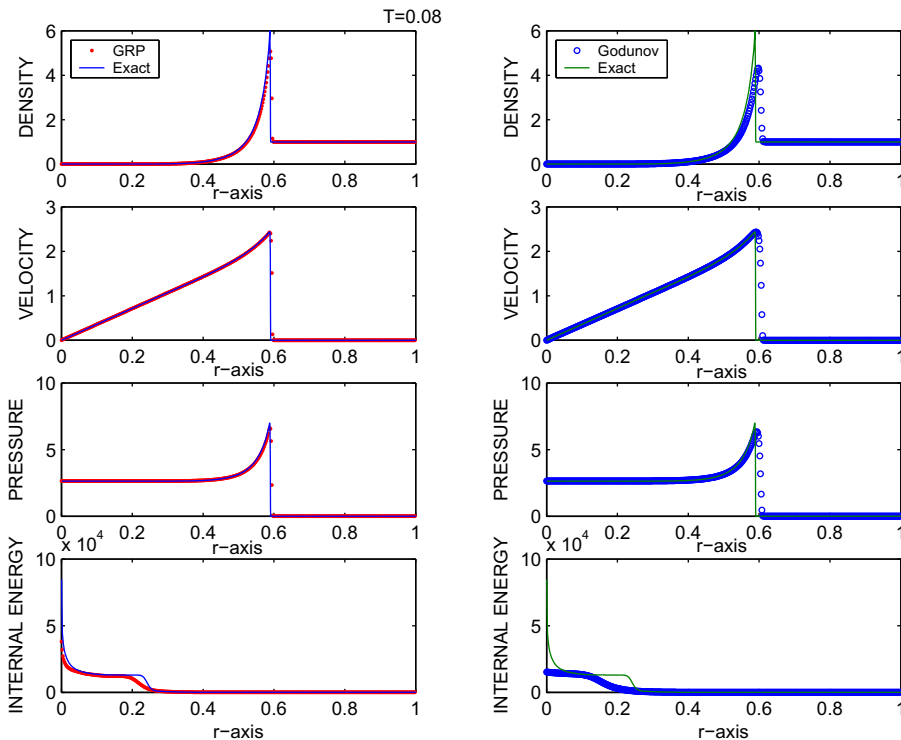


Fig. 6.3. Numerical results for the Sedov-Taylor blast wave problem: 500 grids are used, $\alpha = 1.5$. Left column is the GRP solution; and the right-column is the Godunov solution.

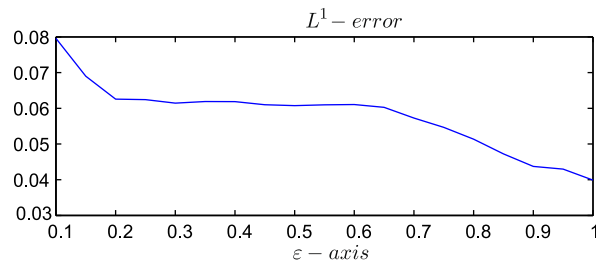


Fig. 6.4. L^1 -error estimate for the Sedov–Taylor blast wave problem at $T = 0.08$.

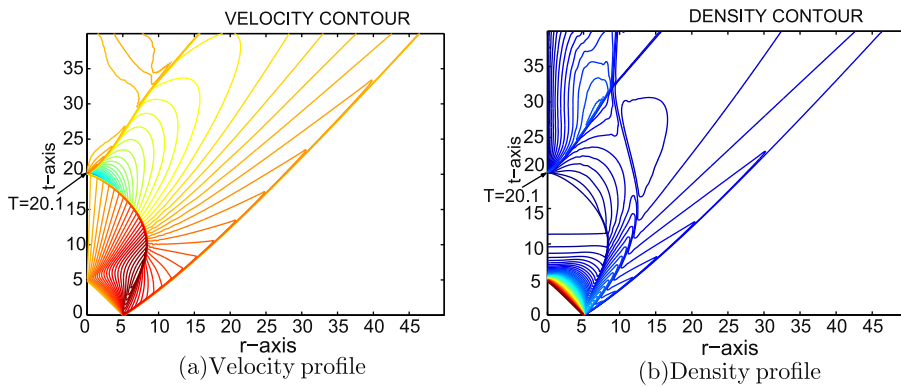


Fig. 6.5. The contour curves of velocity and density for the spherical explosion projected onto the (r, T) plane: 500 grids are used, $\alpha = 1.4$.

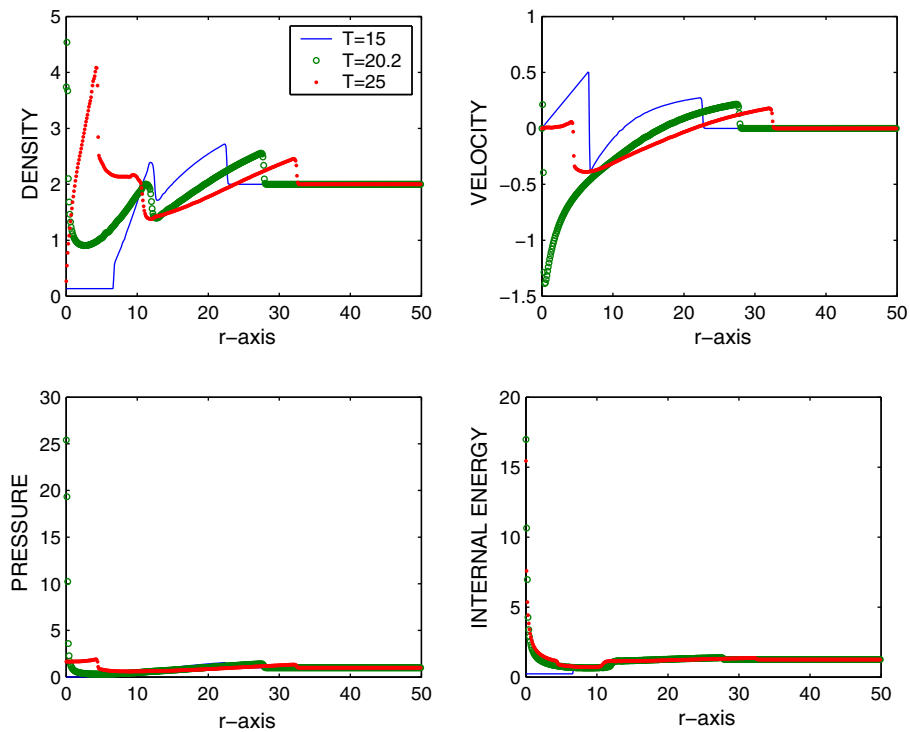


Fig. 6.6. Numerical results for the spherical explosion at different times: 500 grids are used, $\alpha = 1.4$.

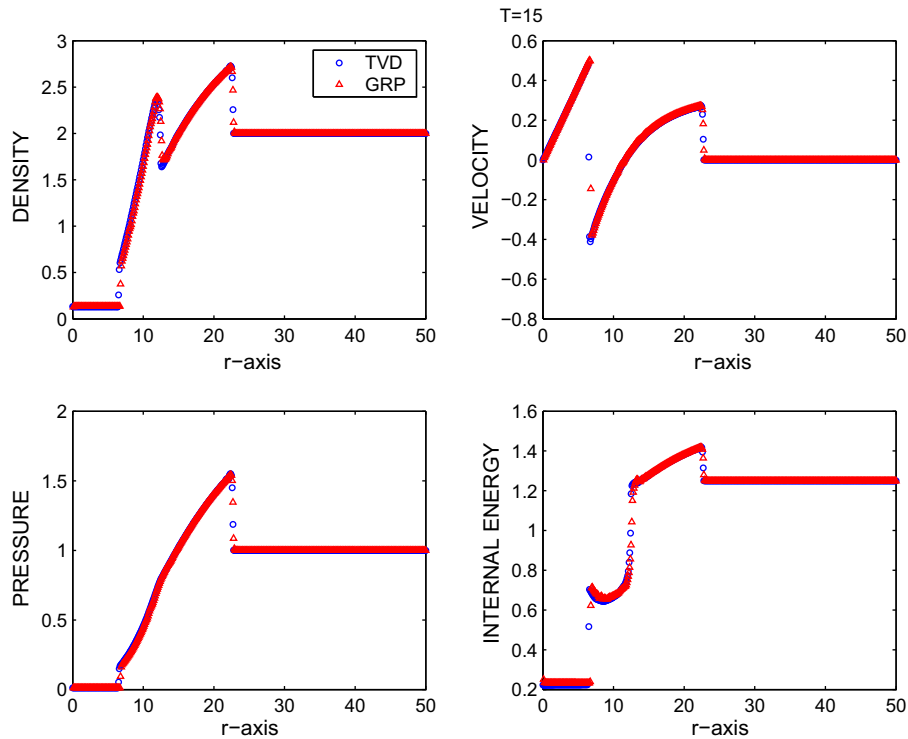


Fig. 6.7. Comparison with the result by the modified Harten's TVD scheme for the spherical explosion problem at time $T=15$: 500 grids are used.

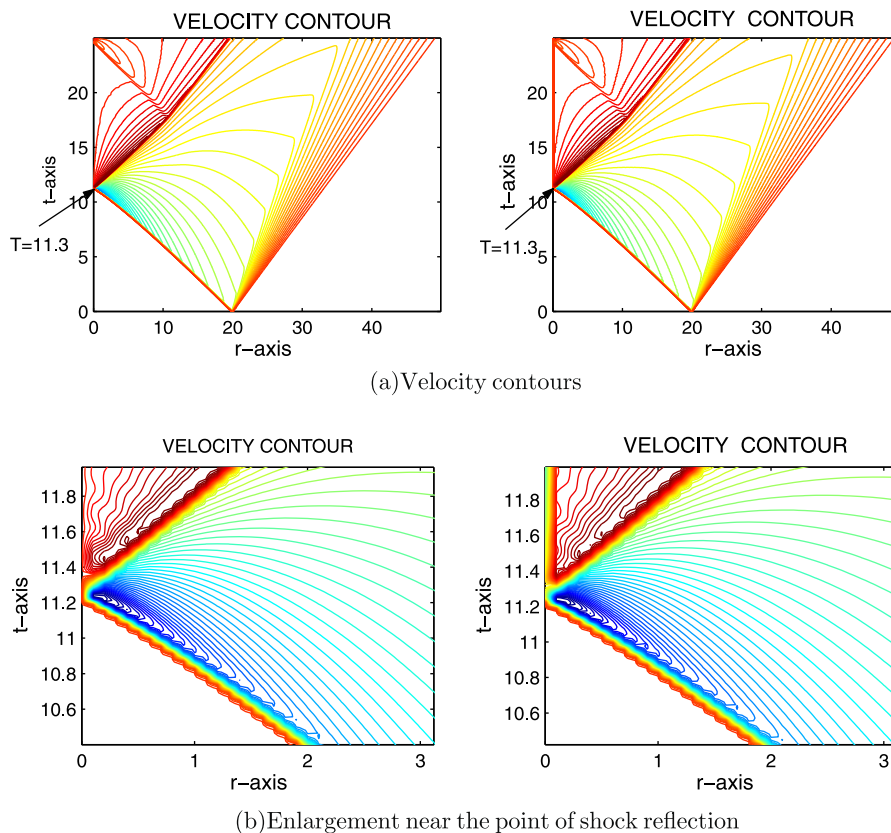


Fig. 6.8. The contour curves of velocity for cylindrical implosion projected onto the (r, T) -plane. Left column is obtained with the current proposed boundary condition; right column is obtained with the reflection boundary condition.

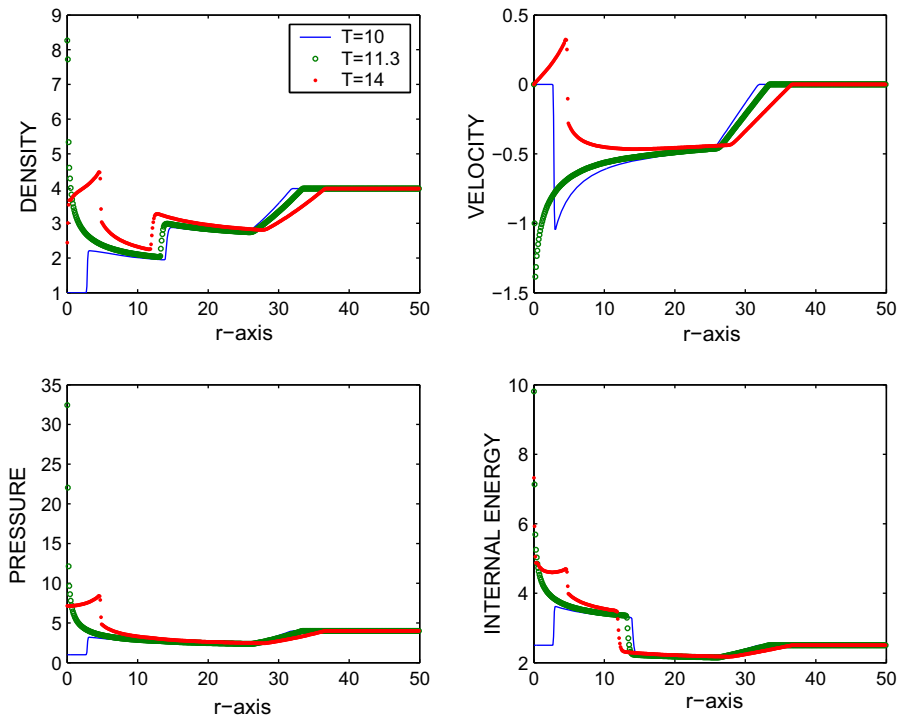


Fig. 6.9. Numerical results by the current GRP scheme for cylindrical implosion at different times: 500 grids are used, $\alpha = 1.9$.

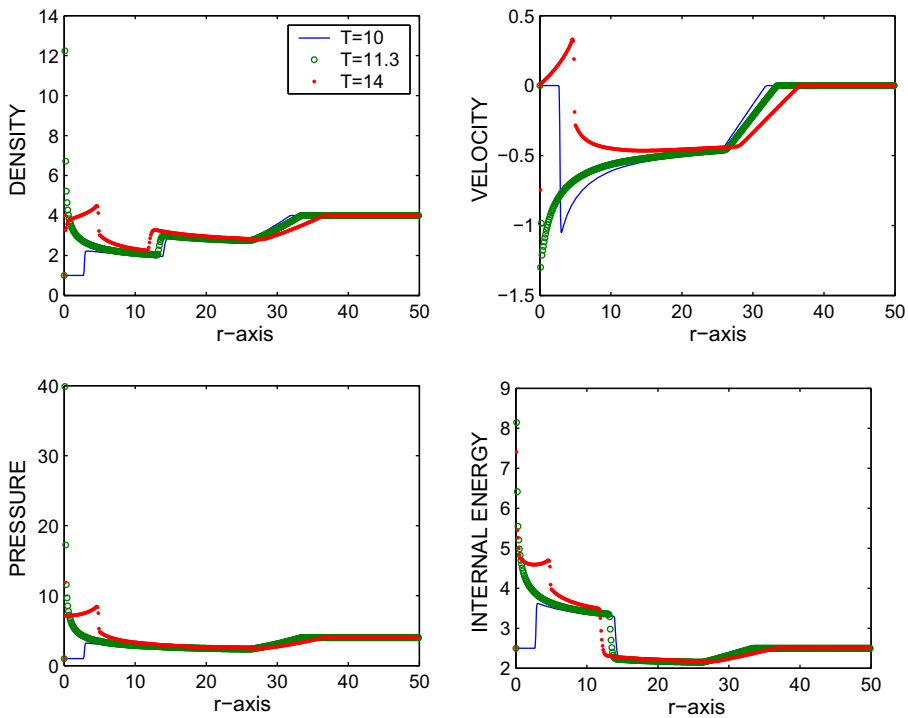


Fig. 6.10. Numerical results by the current GRP scheme for cylindrical implosion with the reflection boundary condition.

and propagates outwards with the expanding gas. However, its strength increases with time and reaches a fairly high intensity in a short time, stops propagating outwards soon and reverts backwards to implode on the center. Fig. 6.5 has clearly exhibited the trajectory of the second shock. It shows that the second shock forms at the non-dimensional time about

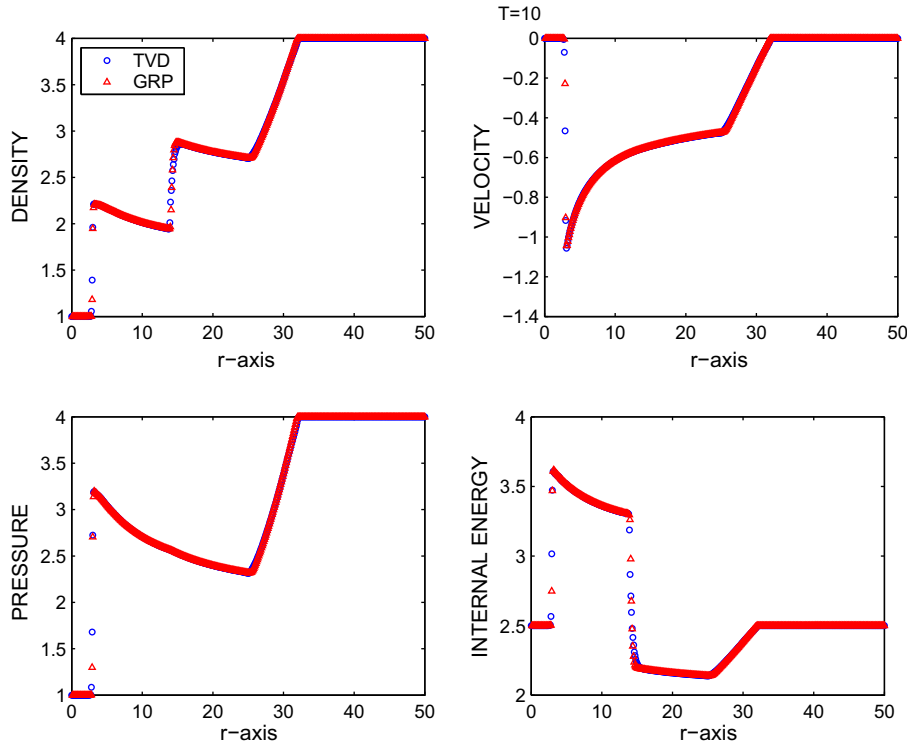


Fig. 6.11. Comparison with the result by the modified Harten's TVD scheme for the cylindrical implosion problem at time $T = 10$: 500 grid points are used.

$T = 3.2$, stops outward motion at the non-dimensional time about $T = 9.5$ and finally implodes at the center at the non-dimensional time about $T = 20.1$. To look at the details of the flow, Fig. 6.6 displays the profiles of flow density, velocity, pressure and internal energy at three different instants. As shown, at $T = 15$, the second shock has formed and is moving inwards to the location about $r = 6.0$. Just after the implosion of the second shock at the center at $T = 20.2$, the pressure and internal energy (thus temperature) at the center increase greatly (please look at the profiles indicated with symbol “circle” in Fig. 6.6). After the implosion and reflection of the shock at the center, a reflected shock is generated and moves outwards with a rapid decrease of strength as shown in Fig. 6.6 at $T = 25.0$. The reflected shock will interacting with the moving contact discontinuity and even more complex physics will occurs as discussed in [23]. The present work stops computation at $T = 30.0$.

We compare the current result with that by the modified Harten's TVD scheme [23] in Fig. 6.7. That method uses an artificial compression technique to enhance the resolution of the material interface (contact discontinuities in the present context). By comparison, we clearly observe that the two results agree quite well in addition that the present GRP method gives a slightly better resolution to discontinuities.

6.4. The numerical simulation of cylindrical implosion

In the process of simulation of cylindrical implosion, we choose the same model as in [18,1,30,23]. The gas is initially at rest with non-dimensional $\rho = 1, p = 1$ for $0 \leq r \leq 20$ and $\rho = 4, p = 4$ for $20 < r \leq 50$.

For this kind of problems, when the diaphragm separating the high and low pressure region is suddenly broken, there is an inward converging shock wave in the low pressure region, a rarefaction wave moving out into the high pressure region with a moving-in contact discontinuity separating the rarefaction wave and the shock wave. The moving-in shock with a rapid increase of its strength soon implodes and reflects at the center. Fig. 6.8(left) records the time history of velocity profile. From this figure, it is clearly shown that the shock wave moves inwards and implodes at the center at the time about $T = 11.3$. Fig. 6.9 shows a series of plots of flow density, velocity, pressure and internal energy at three time stages. The shock wave with an increasing strength converges towards the center at $T = 10.0$ and makes implosion at the center at $T = 11.3$. Because of the implosion, the pressure increases rapidly to a large but finite value. The temperature and density at the center also attain their maximum values at the same time. After its implosion, the shock wave is reflected outwards with a decrease of its strength as shown in Fig. 6.9 at $T = 14.0$. Subsequent shock wave interaction with the moving contact discontinuity and implosion at the center can occur many times as discussed in [23]. In the present study, we stopped the computation at $T = 20.0$.

As comparison, we provide a numerical solution obtained with the reflection boundary condition [17] at the center $r = 0$. In Fig. 6.8, we compare the solutions via the velocity contours. In Fig. 6.8(a), we observe that some oscillations of velocity profile are present near the center if the reflection boundary condition is used. The current proposed boundary condition can avoid the oscillations effectively. Furthermore, the phenomenon of the time delay is observed at the moment that the shock wave implodes at the center, see Fig. 6.8(b). That is, there is an interval between the implosion time and the reflection time of the shock wave at the center. In Fig. 6.10, we display the complete solution with the reflection boundary condition so as to compare with Fig. 6.9 by the GRP scheme with the current boundary condition.

Similar to the case of explosion, we had compared the present GRP result with that obtained by the modified Harten's TVD scheme for this case. See Fig. 6.11.

Acknowledgments

We thank the referees' careful reading and comments, which substantially improves the present paper. We also thank Matania Ben-Artzi for his interest and discussion. Jiequan Li's research is supported by 973 Project with No. 2006CB805902 and PHR(IHLB), Fok Ying Tong Education Foundation and the Key Program from Beijing Educational Commission with no. KZ200910028002. Tiegang Liu's research is supported by NSFC with No. 10871018.

Appendix A. Notations

In Table 1, we list some notations used in this paper.

Appendix B. Basic differential relations for fluid flows

To resolve curved rarefaction waves, we need to use the concept of Riemann invariants and provide some differential relations among different variables. For more details, we can refer to [8].

For this purpose, we write the system of Euler equations (2.1) in the following form:

$$\frac{D\rho}{Dt} + \rho \frac{\partial u}{\partial r} = -\frac{m-1}{r} \rho u, \quad \rho \frac{Du}{Dt} + \frac{\partial p}{\partial r} = 0, \quad \frac{DS}{Dt} = 0, \quad (\text{B.1})$$

where $D/Dt = \partial/\partial t + u\partial/\partial r$ is the material derivative, and the entropy S is related to the other variables through the second law of thermodynamics

$$de = TdS + \frac{p}{\rho^2} d\rho, \quad (\text{B.2})$$

and T is the temperature. Regard p as a function of ρ and S , $p = p(\rho, S)$. Then the local sound speed c is defined as

$$c^2 = \frac{\partial p(\rho, S)}{\partial \rho}. \quad (\text{B.3})$$

Thus the first or third equation of (B.1) can be replaced equivalently by

$$\frac{Dp}{Dt} + \rho c^2 \frac{\partial u}{\partial r} = -\frac{m-1}{r} \rho c^2 u. \quad (\text{B.4})$$

Observe that the entropy S is constant along a streamline. Introduce the Riemann invariants ϕ and Ψ ,

Table 1
Basic notations.

Symbols	Definitions
ρ, u, p, S	Density, velocity, pressure, entropy
ϕ, Ψ	Riemann invariants
Q_L, Q_R	$\lim Q(r, 0)$ as $r \rightarrow r_0^-$, $r \rightarrow r_0^+$
Q_L^*, Q_R^*	Constant slopes $\partial Q/\partial r$ for $r < r_0$, $r > r_0$
$R^A(\cdot; Q_L, Q_R)$	Solution of the Riemann problem subject to data Q_L, Q_R
Q_*	$R^A(0; Q_L, Q_R)$
Q_1, Q_2	The value of Q to the left, the right of contact discontinuity
$(\partial Q/\partial t)_*$	$(\partial Q/\partial t)(r, t)$ at $r = r_0$ as $t \rightarrow 0_+$
DQ/Dt	The material derivative of Q , $\partial Q/\partial t + u \cdot \partial Q/\partial r$
$(DQ/Dt)_*$	The limiting value of DQ/Dt at $r = r_0$ as $t \rightarrow 0_+$
$u - c, u, u + c$	Three eigenvalues
β, α	Two characteristic coordinates
σ_L, σ_R	Shock speed at time zero, corresponding to $u - c, u + c$
$\mu^2 = (\gamma - 1)/(\gamma + 1)$	$\gamma > 1$ the polytropic index, $\gamma = 1.4$ for air

$$\phi = u - \int^{\rho} \frac{c(\omega, S)}{\omega} d\omega, \quad \Psi = u + \int^{\rho} \frac{c(\omega, S)}{\omega} d\omega. \quad (\text{B.5})$$

Recall [6] that along the characteristic $C_+ : dr/dt = u + c$ we have

$$d\Psi = K(\rho, S)dS - \frac{m-1}{r}cudt, \quad dS = c \frac{\partial S}{\partial r} dt, \quad (\text{B.6})$$

and, along $C_- : dr/dt = u - c$,

$$d\phi = -K(\rho, S)dS + \frac{m-1}{r}cudt, \quad dS = -c \frac{\partial S}{\partial r} dt. \quad (\text{B.7})$$

In particular, in the important case of polytropic gases, we have

$$p = (\gamma - 1)\rho e, \quad \gamma > 1, \quad (\text{B.8})$$

where e is a function of S alone. Then the Riemann invariants are

$$\phi = u - \frac{2c}{\gamma - 1}, \quad \Psi = u + \frac{2c}{\gamma - 1}, \quad (\text{B.9})$$

where $c^2 = \gamma p / \rho$. In this case, we have

$$K(\rho, S) = \frac{1}{(\gamma - 1)\rho c} \frac{\partial p}{\partial S} = \frac{T}{c}, \quad (\text{B.10})$$

and

$$\begin{aligned} d\phi &= du - \frac{\gamma}{(\gamma - 1)\rho c} dp + \frac{c}{(\gamma - 1)\rho} d\rho, & d\Psi &= du + \frac{\gamma}{(\gamma - 1)\rho c} dp - \frac{c}{(\gamma - 1)\rho} d\rho, \\ TdS &= \frac{dp}{(\gamma - 1)\rho} - \frac{c^2}{(\gamma - 1)\rho} d\rho. \end{aligned} \quad (\text{B.11})$$

Appendix C. The Rankine–Hugoniot relations for shocks

Let $r = r(t)$ be the shock trajectory with speed $\sigma = dr/dt$,

$$\sigma = \frac{\rho u - \bar{\rho} \bar{u}}{\rho - \bar{\rho}}, \quad (\text{C.1})$$

where we assume that $(\bar{\rho}, \bar{u}, \bar{p})$ and (ρ, u, p) are the states on the wave front and behind the wave back. Then across the shock, the (p, u) Rankine–Hugoniot relations are written in the form

$$u = \bar{u} \pm H(p; \bar{p}, \bar{\rho}), \quad (\text{C.2})$$

where the plus sign refers to the shock associated with $u + c$, while the minus sign to $u - c$. The (ρ, p) Rankine–Hugoniot relation is

$$\rho = G(p; \bar{p}, \bar{\rho}). \quad (\text{C.3})$$

Denote

$$H_1(p; \bar{p}, \bar{\rho}) = \frac{\partial H}{\partial p}, \quad H_2(p; \bar{p}, \bar{\rho}) = \frac{\partial H}{\partial \bar{p}}, \quad H_3(p; \bar{p}, \bar{\rho}) = \frac{\partial H}{\partial \bar{\rho}}, \quad (\text{C.4})$$

and

$$G_1(p; \bar{p}, \bar{\rho}) = \frac{\partial G}{\partial p}, \quad G_2(p; \bar{p}, \bar{\rho}) = \frac{\partial G}{\partial \bar{p}}, \quad G_3(p; \bar{p}, \bar{\rho}) = \frac{\partial G}{\partial \bar{\rho}}. \quad (\text{C.5})$$

For the polytropic gases, we have

$$\begin{aligned} H(p; \bar{p}, \bar{\rho}) &= (p - \bar{p}) \sqrt{\frac{1 - \mu^2}{\bar{\rho}(p + \mu^2 \bar{p})}}, & H_1(p; \bar{p}, \bar{\rho}) &= \frac{1}{2} \sqrt{\frac{1 - \mu^2}{\bar{\rho}(p + \mu^2 \bar{p})}} \cdot \frac{p + (1 + 2\mu^2)\bar{p}}{p + \mu^2 \bar{p}}, \\ H_2(p; \bar{p}, \bar{\rho}) &= -\frac{1}{2} \sqrt{\frac{1 - \mu^2}{\bar{\rho}(p + \mu^2 \bar{p})}} \cdot \frac{(2 + \mu^2)p + \mu^2 \bar{p}}{p + \mu^2 \bar{p}}, & H_3(p; \bar{p}, \bar{\rho}) &= -\frac{p - \bar{p}}{2\bar{\rho}} \sqrt{\frac{1 - \mu^2}{\bar{\rho}(p + \mu^2 \bar{p})}}. \end{aligned} \quad (\text{C.6})$$

and

$$\begin{aligned} G(p; \bar{p}, \bar{\rho}) &= \bar{\rho} \frac{p + \mu^2 \bar{p}}{\bar{p} + \mu^2 p}, & G_1(p; \bar{p}, \bar{\rho}) &= \frac{\bar{\rho}(1 - \mu^4) \bar{p}}{(\bar{p} + \mu^2 p)^2}, \\ G_2(p; \bar{p}, \bar{\rho}) &= \frac{\bar{\rho}(\mu^4 - 1)p}{(\bar{p} + \mu^2 p)^2}, & G_3(p; \bar{p}, \bar{\rho}) &= \frac{p + \mu^2 \bar{p}}{\bar{p} + \mu^2 p}. \end{aligned} \quad (\text{C.7})$$

Appendix D. Derivation of linear equations in Propositions 4.1 and 4.6

Here we want to derive the pair of linear Eq. (4.4) in Proposition 4.1 and the linear Eq. (4.7) in Proposition 4.6, which are obtained by solving the generalized Riemann problem.

D.1. Derivation of linear Eq. (4.4)

The derivation of (4.4) is equivalent to the following proposition.

Proposition D.1 (Nonsonic case). *Assume that the t -axis is located inside the intermediate region. Then the limiting values $(Du/Dt)_*$ and $(Dp/Dt)_*$ as $t \rightarrow 0+$ are obtained by solving a pair of linear algebraic equations*

$$\begin{aligned} a_L \left(\frac{Du}{Dt} \right)_* + b_L \left(\frac{Dp}{Dt} \right)_* &= d_L, \\ a_R \left(\frac{Du}{Dt} \right)_* + b_R \left(\frac{Dp}{Dt} \right)_* &= d_R, \end{aligned} \quad (\text{D.1})$$

where a_L, a_R, b_L, b_R, d_L and d_R are summarized for all cases in Appendix E, respectively.

Proof. We consider a typical wave configuration in Fig. D.1, the rarefaction wave moves to the left and the shock moves to the right, separated by a contact discontinuity with the speed u . The other cases can be treated similarly. The proof is divided into two parts: The resolution of the rarefaction wave associated with $u - c$, and the shock wave associated with $u + c$.

A. The resolution of rarefaction waves: Consider the rarefaction wave associated with $u - c$ and denote by $U_-(r, t)$ (resp. $U_1(r, t)$) the states (regions of smooth flows) ahead (resp. behind) the rarefaction wave, see Fig. D.1(a), where $U_-(r, t)$ is determined by the left initial data $U_L + U'_L(r - r_0)$. Characteristic curves throughout the rarefaction wave are denoted by

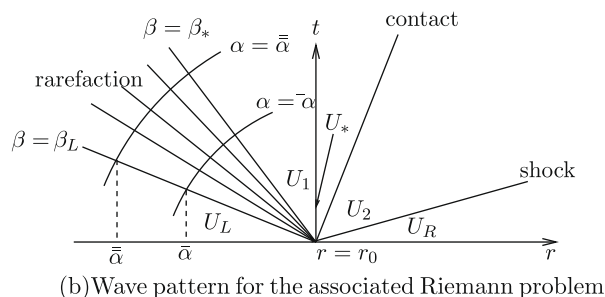
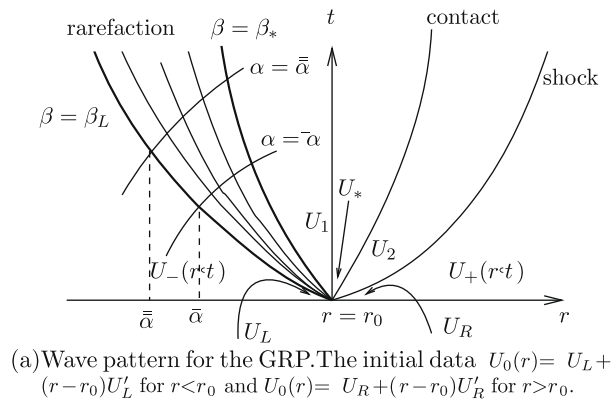


Fig. D.1. Typical wave configuration.

$\beta(r, t) = \beta$ and $\alpha(r, t) = \alpha, \beta \in [\beta_L, \beta_*], -\infty \leq \alpha < 0, \beta_L = u_L - c_L, \beta_* = u_* - c_*$. They are the integral curves of the following equations, respectively:

$$\frac{dr}{dt} = u - c, \quad \frac{dr}{dt} = u + c. \quad (\text{D.2})$$

Here β and α are denoted as follows: β is the initial value of the slope $u - c$ at the singularity $(r, t) = (r_0, 0)$, and α for the transversal characteristic curves is the r -coordinate of the intersection point with the leading β -curve, which may be properly normalized for polytropic gases. Then the coordinates (r, t) can be expressed as

$$r = r(\alpha, \beta), \quad t = t(\alpha, \beta), \quad (\text{D.3})$$

which satisfy

$$\frac{\partial r}{\partial \alpha} = (u - c) \frac{\partial t}{\partial \alpha}, \quad \frac{\partial r}{\partial \beta} = (u + c) \frac{\partial t}{\partial \beta}. \quad (\text{D.4})$$

Differentiating the first equation in (D.4) with respect to β , the second with respect to α , and subtracting, we see that the function $t = t(\alpha, \beta)$ satisfies,

$$2c \frac{\partial^2 t}{\partial \alpha \partial \beta} = -\frac{\partial(u + c)}{\partial \alpha} \cdot \frac{\partial t}{\partial \beta} + \frac{\partial(u - c)}{\partial \beta} \cdot \frac{\partial t}{\partial \alpha}, \quad (\text{D.5})$$

and the characteristic equations for Ψ and S in (B.6) become

$$\frac{\partial S}{\partial \beta} = \frac{\partial t}{\partial \beta} \cdot c \frac{\partial S}{\partial r}, \quad \frac{\partial \Psi}{\partial \beta} = \frac{\partial t}{\partial \beta} \cdot \left(cK(\rho, S) \frac{\partial S}{\partial r} - \frac{m-1}{r} cu \right). \quad (\text{D.6})$$

Note that for the general (curved) rarefaction wave, see Fig. D.1(a), we have

$$\frac{\partial(u - c)}{\partial \beta}(0, \beta) = 1, \quad \frac{\partial t}{\partial \beta}(0, \beta) \equiv 0, \quad \beta_L \leq \beta \leq \beta_*. \quad (\text{D.7})$$

Denote

$$t_{\text{ass}}(\alpha, \beta) = \frac{\alpha}{(\Psi_L - \beta)^{\frac{1}{2\mu^2}}}, \quad r_{\text{ass}}(\alpha, \beta) = \frac{\alpha\beta}{(\Psi_L - \beta)^{\frac{1}{2\mu^2}}}, \quad \mu^2 = \frac{\gamma - 1}{\gamma + 1}, \quad (\text{D.8})$$

where $-\infty < \alpha \leq 0, \beta_L := u_L - c_L \leq \beta \leq \beta_* := u_* - c_*$ and $\Psi_L = u_L + \frac{2c_L}{\gamma-1}$. Then the coordinates (r, t) inside the rarefaction wave can be expressed as

$$t(\alpha, \beta) = t_{\text{ass}}(\alpha, \beta) + O(\alpha^2), \quad r(\alpha, \beta) = r_0 + r_{\text{ass}}(\alpha, \beta) + O(\alpha^2), \quad \text{as } \alpha \rightarrow 0. \quad (\text{D.9})$$

Then the characteristic map $T : (\alpha, \beta) \rightarrow (r, t)$ transforms the domain $\{(\alpha, \beta) | -\infty < \alpha \leq 0, \beta_L \leq \beta \leq \beta_*\}$ onto the rarefaction fan, and the segment $\alpha = 0, \beta_L \leq \beta \leq \beta_*$ corresponds to the singularity point $(r, t) = (r_0, 0)$. The leading term $(r_{\text{ass}}, t_{\text{ass}})$ determines the local solution structure.

We use (B.1), (B.4) and (B.6) to yield

$$\frac{Du}{Dt} + \frac{1}{\rho c} \frac{Dp}{Dt} = \frac{D\Psi}{Dt}. \quad (\text{D.10})$$

So we need to compute $D\Psi/Dt$ at $(0, \beta)$. From (B.6) we have

$$\frac{D\Psi}{Dt} = cK(\rho, S) \frac{\partial S}{\partial r} - c \frac{\partial \Psi}{\partial r} - \frac{m-1}{r} cu. \quad (\text{D.11})$$

Denote

$$A(\alpha, \beta) := cK(\rho, S) \cdot \frac{\partial S}{\partial r}(\alpha, \beta), \quad B(\alpha, \beta) := A(\alpha, \beta) - \frac{m-1}{r} cu. \quad (\text{D.12})$$

Then we just need to compute $A(0, \beta)$ and $c(0, \beta) \frac{\partial \Psi}{\partial r}(0, \beta)$ separately. Compared to the 1-D planar flows, there is an extra term caused by the geometrical source term:

(i) The computation of $A(0, \beta)$. The detail is exactly the same with the corresponding part of Lemma 3.1 in [8]. There holds,

$$A(0, \beta) = K(\rho(0, \beta), S_L) \cdot \left(\frac{\partial t_{\text{ass}}}{\partial \alpha} \right)^{-1}(0, \beta) \left(\frac{\partial t_{\text{ass}}}{\partial \alpha} \right)(0, \beta_L) \cdot c_L S'_L \exp \left(- \int_{\beta_L}^{\beta} \frac{1}{2c(0, \xi)} d\xi \right). \quad (\text{D.13})$$

For the polytropic gases, we have,

$$A(0, \beta) = \left(\frac{c}{c_L} \right)^{(1+\mu^2)/\mu^2} T_L S'_L, \quad (\text{D.14})$$

where $T_L S'_L$ is given by (B.11).

(ii) The computation of $c(0, \beta) \cdot \frac{\partial \Psi}{\partial r}(0, \beta)$. As in [8], we observe that

$$c(0, \beta) \frac{\partial \Psi}{\partial r}(0, \beta) = -\frac{1}{2} \left[\left(\frac{\partial t_{ass}}{\partial \alpha} \right)^{-1}(0, \beta) \cdot \frac{\partial \Psi}{\partial \alpha}(0, \beta) - B(0, \beta) \right]. \quad (D.15)$$

Note that $A(0, \beta)$, as function of β , is already known in (D.13), so we obtain $B(0, \beta)$ from (D.12). Therefore we are left with the calculation of $(\partial \Psi / \partial \alpha)(0, \beta)$. The characteristic equation for Ψ in (D.6) gives

$$\frac{\partial^2 \Psi}{\partial \alpha \partial \beta} = \frac{\partial^2 t}{\partial \alpha \partial \beta} \cdot B(\alpha, \beta) + \frac{\partial t}{\partial \beta} \frac{\partial B(\alpha, \beta)}{\partial \alpha}. \quad (D.16)$$

Setting $\alpha = 0$ and recalling (D.5) and (D.7), we obtain

$$\frac{\partial}{\partial \beta} \left(\frac{\partial \Psi}{\partial \alpha}(0, \beta) \right) = \frac{1}{2c(0, \beta)} \cdot \frac{\partial t_{ass}}{\partial \alpha}(0, \beta) \cdot B(0, \beta). \quad (D.17)$$

The integration from β_L to β and the substitution of $B(0, \beta)$ by $A(0, \beta)$ give,

$$\frac{\partial \Psi}{\partial \alpha}(0, \beta) = \frac{\partial \Psi}{\partial \alpha}(0, \beta_L) + \int_{\beta_L}^{\beta} \frac{1}{2c(0, \zeta)} \cdot \frac{\partial t_{ass}}{\partial \alpha}(0, \zeta) \cdot A(0, \zeta) d\zeta - \frac{m-1}{2r_0} \int_{\beta_L}^{\beta} u(0, \zeta) \cdot \frac{\partial t_{ass}}{\partial \alpha}(0, \zeta) d\zeta, \quad (D.18)$$

where $(\partial \Psi / \partial \alpha)(0, \beta_L)$ is obtained from (D.15) by setting $\beta = \beta_L$ and $(\partial \Psi / \partial r)(0, \beta_L) = \Psi'_L$.

For the polytropic gases, we have

$$u = \mu^2 \Psi_L + (1 - \mu^2) \beta, \quad c = \mu^2 (\Psi_L - \beta), \quad (D.19)$$

By using (D.8), (D.14) and (D.19) and noting $T/T_L = c^2/c_L^2$, we obtain

$$\frac{\partial \Psi}{\partial \alpha}(0, \beta) = \frac{\partial \Psi}{\partial \alpha}(0, \beta_L) - \frac{B_L}{1 + 2\mu^2} \left(c^{(1+2\mu^2)/(2\mu^2)} - c_L^{(1+2\mu^2)/(2\mu^2)} \right) + \frac{m-1}{2r_0} \chi_L(\beta). \quad (D.20)$$

where B_L , $\Psi_\alpha(0, \beta_L)$, $\chi_L(\beta)$ are given by

$$\begin{aligned} B_L &= (\mu^2)^{1/(2\mu^2)} c_L^{-(\mu^2+1)/\mu^2} T_L S'_L, \\ \Psi_\alpha(0, \beta_L) &= (\Psi_L - \beta_L)^{-\frac{1}{2\mu^2}} \left[T_L S'_L - \frac{m-1}{r_0} c_L u_L - 2c_L \Psi'_L \right], \quad \Psi'_L = u'_L + \frac{2c'_L}{\gamma-1}, \\ \chi_L(\beta) &= \begin{cases} 2\mu^2(E_L(\beta) - E_L(\beta_L)), & \text{if } \gamma \neq \frac{5}{3}, \gamma \neq 3, \\ c_L - c + \Psi_L \log\left(\frac{c}{c_L}\right), & \text{if } \gamma = 3, \\ -\frac{3}{4} \log\left(\frac{c}{c_L}\right) - \frac{\Psi_L}{4} \left(\frac{1}{c} - \frac{1}{c_L}\right), & \text{if } \gamma = \frac{5}{3}, \end{cases} \end{aligned} \quad (D.21)$$

and

$$E_L(\beta) = (\Psi_L - \beta)^{-\frac{1}{2\mu^2}} \left[\frac{(\mu^2 - 1)}{4\mu^2 - 1} (\Psi_L - \beta)^2 + \frac{\Psi_L}{2\mu^2 - 1} (\Psi_L - \beta) \right]. \quad (D.22)$$

Then we obtain $c(0, \beta) \frac{\partial \Psi}{\partial r}(0, \beta)$ by combining (D.20) with (D.15).

Inserting (D.14) and (D.15) into (D.11), we obtain the value $D\Psi/Dt(0, \beta)$, as given in d_L (for the polytropic gases). Thus we obtain the first equation in (D.1).

B. The resolution of shocks: We take along the shock trajectory the differentiation $(\frac{\partial}{\partial t} + \sigma \frac{\partial}{\partial r})\Gamma = 0$ for $\Gamma = u - \bar{u} - H(p, \bar{p}, \bar{\rho})$ to obtain

$$\frac{\partial u}{\partial t} + \sigma \frac{\partial u}{\partial r} = \frac{\partial \bar{u}}{\partial t} + \sigma \frac{\partial \bar{u}}{\partial r} + \frac{\partial H}{\partial p} \cdot \left(\frac{\partial p}{\partial t} + \sigma \frac{\partial p}{\partial r} \right) + \frac{\partial H}{\partial \bar{p}} \cdot \left(\frac{\partial \bar{p}}{\partial t} + \sigma \frac{\partial \bar{p}}{\partial r} \right) + \frac{\partial H}{\partial \bar{\rho}} \cdot \left(\frac{\partial \bar{\rho}}{\partial t} + \sigma \frac{\partial \bar{\rho}}{\partial r} \right). \quad (D.23)$$

Using (B.1) and (B.4), we have

$$\begin{aligned} \frac{\partial u}{\partial t} + \sigma \frac{\partial u}{\partial r} &= \frac{Du}{Dt} - \frac{1}{\rho c^2} (\sigma - u) \frac{Dp}{Dt} - \frac{m-1}{r_0} (\sigma - u) u, \\ \frac{\partial p}{\partial t} + \sigma \frac{\partial p}{\partial r} &= \frac{Dp}{Dt} - \rho (\sigma - u) \frac{Du}{Dt}. \end{aligned} \quad (D.24)$$

Then we use (B.1) and (B.4) again to replace the time derivatives of \bar{p} , $\bar{\rho}$ by the corresponding space derivatives and proceed to take the limit $t \rightarrow 0+$ for the resulting equation to finally obtain the second equation in (D.1). \square

D.2. Derivation of linear Eq. (4.7)

We still take the wave configuration in Fig. D.1. As $u_* > 0$, we calculate $(\partial\rho/\partial t)_*$ from the rarefaction wave side. Use the state equation $p = p(\rho, S)$ and the fact $\frac{\partial S}{\partial t} = -u \frac{\partial S}{\partial r}$ to obtain

$$\frac{\partial p}{\partial t} = c^2 \frac{\partial \rho}{\partial t} + \frac{\partial p}{\partial S} \frac{\partial S}{\partial t} = c^2 \frac{\partial \rho}{\partial t} - u \frac{\partial p}{\partial S} \frac{\partial S}{\partial r}. \quad (\text{D.25})$$

Then we set $(\alpha, \beta) = (0, \beta_*)$ to arrive at

$$c_{1*}^2 \left(\frac{\partial \rho}{\partial t} \right)_* - \left(\frac{\partial p}{\partial t} \right)_* = \frac{\partial p}{\partial S}(\rho_{1*}, S_*) \cdot \frac{u_*}{c_{1*} K(\rho_{1*}, S_*)} A(0, \beta_*), \quad (\text{D.26})$$

where $A(0, \beta_*)$ is given in (D.13). For the polytropic gases, we have

$$c_{1*}^2 \left(\frac{\partial \rho}{\partial t} \right)_* - \left(\frac{\partial p}{\partial t} \right)_* = (\gamma - 1) \rho_{1*} u_* \left(\frac{c_{1*}}{c_L} \right)^{(1+\mu^2)/\mu^2} T_L S'_L. \quad (\text{D.27})$$

As $u_* < 0$, we take along the shock trajectory $r = r(t)$ the differentiation $(\frac{\partial}{\partial t} + \sigma \frac{\partial}{\partial r}) \Gamma = 0$ for $\Gamma = \rho - G(\rho; \bar{p}, \bar{\rho})$, exactly as was done in the proof of Lemma 4.1 in [8, pp. 28–29]. Then we obtain the formula

$$g_\rho^{Rshock} \left(\frac{\partial \rho}{\partial t} \right)_* + g_p^{Rshock} \left(\frac{\partial p}{\partial t} \right)_* + g_u^{Rshock} \left(\frac{\partial u}{\partial t} \right)_* = f^{Rshock}, \quad (\text{D.28})$$

where $g_\rho^{Rshock}, g_p^{Rshock}, g_u^{Rshock}$ and f^{Rshock} are given in (E.10).

Also we remark that if $u_* = 0$, we can use either (D.26) or (D.28).

Appendix E. Useful coefficients for the GRP scheme

We collect in Table 2 for all cases the coefficients of the system of the linear algebraic equations in Proposition 4.1 and in Table 3 for Proposition 4.6 for the polytropic gases. Here we assume that the t -axis (cell interface) is located inside the intermediate region. In these tables, the 1-shock (resp. 3-shock) refers to the shock associated with the $u - c$ characteristic family (resp. $u + c$). Analogously for the 1-rarefaction wave and the 3-rarefaction wave.

Below we denote $J = L$ or R . For example, as $J = L$, Q_J represents the value of Q taken from the left. And particularly, we denote $(\rho_{L*}, c_{L*}) = (\rho_{1*}, c_{1*})$ and $(\rho_{R*}, c_{R*}) = (\rho_{2*}, c_{2*})$.

E.1. The coefficients in Proposition 4.1 for all cases

The coefficients in Proposition 4.1 are given by

$$h_J = a_J - \rho_* u_* b_J, \quad q_J = b_J - \frac{u_*}{\rho_* c_*^2} a_J, \quad k_J = \frac{m-1}{r_0} u_*^2 h_J + \frac{c_*^2 - u_*^2}{c_*^2} d_J, \quad (\text{E.1})$$

Table 2

Useful coefficients solving linear algebraic equations in Proposition 4.1.

Two rarefaction waves	$(a_L, b_L) = (a_L^{rare}, b_L^{rare}), d_L = d_L^{rare}$ $(a_R, b_R) = (a_R^{rare}, b_R^{rare}), d_R = d_R^{rare}$
Two shocks	$(a_L, b_L) = (a_L^{shock}, b_L^{shock}), d_L = d_L^{shock}$ $(a_R, b_R) = (a_R^{shock}, b_R^{shock}), d_R = d_R^{shock}$
Left shock and right rarefaction wave	$(a_L, b_L) = (a_L^{shock}, b_L^{shock}), d_L = d_L^{shock}$ $(a_R, b_R) = (a_R^{rare}, b_R^{rare}), d_R = d_R^{rare}$
Left rarefaction wave and right shock	$(a_L, b_L) = (a_L^{rare}, b_L^{rare}), d_L = d_L^{rare}$ $(a_R, b_R) = (a_R^{shock}, b_R^{shock}), d_R = d_R^{shock}$

Table 3

Useful coefficients in Proposition 4.6.

$u_* > 0$	Left rarefaction wave	$(g_\rho, g_u, g_p, f) = (g_\rho^{Lrare}, g_u^{Lrare}, g_p^{Lrare}, f^{Lrare})$
	Left shock	$(g_\rho, g_u, g_p, f) = (g_\rho^{Lshock}, g_u^{Lshock}, g_p^{Lshock}, f^{Lshock})$
$u_* < 0$	Right rarefaction wave	$(g_\rho, g_u, g_p, f) = (g_\rho^{Rrare}, g_u^{Rrare}, g_p^{Rrare}, f^{Rrare})$
	Right shock	$(g_\rho, g_u, g_p, f) = (g_\rho^{Rshock}, g_u^{Rshock}, g_p^{Rshock}, f^{Rshock})$

where we denote

$$(\rho_*, c_*) = \begin{cases} (\rho_{1*}, c_{1*}), & \text{for } u_* > 0, \\ (\rho_{2*}, c_{2*}), & \text{for } u_* \leq 0. \end{cases} \quad (\text{E.2})$$

The parameters in (E.1) for rarefaction waves are given by

$$\begin{aligned} (a_L^{\text{rare}}, b_L^{\text{rare}}) &= \left(1, \frac{1}{\rho_{1*} c_{1*}}\right), \quad (a_R^{\text{rare}}, b_R^{\text{rare}}) = \left(1, -\frac{1}{\rho_{2*} c_{2*}}\right), \\ d_J^{\text{rare}} &= \left[\frac{1 + \mu^2}{1 + 2\mu^2} \theta_J^{1/(2\mu^2)} + \frac{\mu^2}{1 + 2\mu^2} \theta_J^{(1+\mu^2)/\mu^2} \right] T_J S_J' + \text{sgn}(J) c_J \left(\eta'(J) + \frac{m-1}{2r_0} u_J \right) \theta_J^{1/(2\mu^2)} + \frac{m-1}{2r_0} c_{J*} [\Phi_J(c_{J*}) + \text{sgn}(J) u_*], \end{aligned} \quad (\text{E.3})$$

where $\theta_L = \frac{c_{1*}}{c_L}$, $\theta_R = \frac{c_{2*}}{c_R}$, and $\Phi_J(c_{J*})$ are given by

$$\Phi_J(c_{J*}) = \begin{cases} \frac{(\mu^2-1)c_{J*}}{\mu^2(4\mu^2-1)} \left(1 - \theta_J^{\frac{1-4\mu^2}{2\mu^2}}\right) - \text{sgn}(J) \frac{\eta(J)}{2\mu^2-1} \left(1 - \theta_J^{\frac{1-2\mu^2}{2\mu^2}}\right), & \text{if } \gamma \neq \frac{5}{3}, \gamma \neq 3, \\ c_J - c_{J*} - \text{sgn}(J) \eta(J) \log \theta_J, & \text{if } \gamma = 3, \\ -2[3c_{J*} \log \theta_J - \text{sgn}(J) \eta(J)(1 - \theta_J)], & \text{if } \gamma = \frac{5}{3}, \end{cases} \quad (\text{E.4})$$

and

$$\text{sgn}(J) = \begin{cases} -1, & \text{for } J = L, \\ 1, & \text{for } J = R, \end{cases} \quad \eta(J) = \begin{cases} \Psi_L, & \text{for } J = L, \\ \phi_R, & \text{for } J = R. \end{cases} \quad (\text{E.5})$$

The parameters in (E.1) for shock waves are given by

$$\begin{aligned} a_J^{\text{shock}} &= 1 + \text{sgn}(J) \rho_{J*} (\sigma_J - u_*) H_1^J, \quad b_J^{\text{shock}} = -\frac{1}{\rho_{J*} c_{J*}^2} (\sigma_J - u_*) - \text{sgn}(J) H_1^J, \\ d_J^{\text{shock}} &= L_p^J p_J' + L_u^J u_J' + L_\rho^J \rho_J' - \frac{m-1}{r_0} L_s^J, \end{aligned} \quad (\text{E.6})$$

where all quantities involved are

$$\begin{aligned} \sigma_J &= \frac{\rho_{J*} u_* - \rho_J u_J}{\rho_{J*} - \rho_J}, \\ L_p^J &= -\frac{1}{\rho_J} + \text{sgn}(J) (\sigma_J - u_J) H_2^J, \quad L_u^J = \sigma_J - u_J - \text{sgn}(J) (\rho_J c_J^2 H_2^J + \rho_J H_3^J), \\ L_\rho^J &= \text{sgn}(J) (\sigma_J - u_J) H_3^J, \quad L_s^J = \text{sgn}(J) (\rho_J u_J c_J^2 H_2^J + \rho_J u_J H_3^J) - (\sigma_J - u_*) u_*, \end{aligned} \quad (\text{E.7})$$

and $H_i^J = H_i(p_*, p_J, \rho_J)$, $i = 1, 2, 3$, H_i is referred to (C.6).

E.2. Sonic case

When the t -axis is located inside the rarefaction wave associated with $u + c$. Then we have

$$\left(\frac{\partial u}{\partial t}\right)_* = d_R^{\text{rare}} + \frac{m-1}{r_0} u_*^2, \quad \left(\frac{\partial p}{\partial t}\right)_* = \rho_* u_* d_R^{\text{rare}}, \quad (\text{E.8})$$

where d_R^{rare} is given in (E.3), and $c_{2*} = -u_*$ in (E.3).

E.3. The coefficients in Proposition 4.6

Here we list the coefficients (g_ρ, g_u, g_p, f) in Proposition 4.6 for all cases.

The coefficients in Table 3 for the rarefaction wave cases are:

$$(g_\rho^{\text{rare}}, g_p^{\text{rare}}, g_u^{\text{rare}}) = (c_{J*}^2, -1, 0), \quad f^{\text{rare}} = (\gamma - 1) \rho_{J*} u_* \left(\frac{c_{J*}}{c_J}\right)^{(1+\mu^2)/\mu^2} T_J S_J'. \quad (\text{E.9})$$

The coefficients Table 3 for shock wave cases are given by

$$\begin{aligned} g_\rho^{\text{shock}} &= (u_* - \sigma_J) \cdot (c_{J*}^2 - u_*^2), \\ g_p^{\text{shock}} &= \sigma_J - u_* G_1^J \cdot [c_{J*}^2 + u_* (\sigma_J - u_*)], \\ g_u^{\text{shock}} &= \rho_{J*} u_* \sigma_J (c_{J*}^2 G_1^J - 1), \quad f^{\text{shock}} = u_* (c_{J*}^2 - u_*^2) \cdot \tilde{f}_J + \frac{m-1}{r_0} u_*^2 g_u^{\text{shock}}, \end{aligned} \quad (\text{E.10})$$

where $G_i^l = G_i(p_*; p_j, \rho_j)$, $i = 1, 2, 3$, $\sigma_j = \frac{\rho_j u_* - \rho_j u_j}{\rho_j - \rho_j}$, and

$$\tilde{f}_j = (\sigma_j - u_j) \cdot G_2^l \cdot p_j' + (\sigma_j - u_j) \cdot G_3^l \cdot \rho_j' - \rho_j \cdot (G_2^l \cdot c_j^2 + G_3^l) \cdot \left(u_j' + \frac{m-1}{r_0} u_j \right). \quad (\text{E.11})$$

The definition of G_i is referred to (C.7).

References

- [1] S. Abarbanel, M. Goldberg, Numerical solution of quasi-conservative hyperbolic system the cylindrical shock problem, *J. Comput. Phys.* 10 (1972) 1–21.
- [2] W.E. Baker, *Explosions in Air*, Wilfred Baker Engineering, San Antonio, 1973.
- [3] M. Ben-Artzi, A. Birman, Computation of reactive duct flows in external fields, *J. Comput. Phys.* 86 (1990) 225–255.
- [4] M. Ben-Artzi, J. Falcovitz, A second-order Godunov-type scheme for compressible fluid dynamics, *J. Comput. Phys.* 55 (1) (1984) 1–32.
- [5] M. Ben-Artzi, J. Falcovitz, An upwind second-order scheme for compressible duct flows, *SIAM J. Sci. Statist. Comput.* 7 (3) (1986) 744–768.
- [6] M. Ben-Artzi, J. Falcovitz, *Generalized Riemann Problems in Computational Gas Dynamics*, Cambridge University Press, 2003.
- [7] M. Ben-Artzi, J. Li, Hyperbolic balance laws: Riemann invariants and the generalized Riemann problem, *Numer. Math.* 106 (3) (2007) 369–425.
- [8] M. Ben-Artzi, J. Li, G. Warnecke, A direct Eulerian GRP scheme for compressible fluid flows, *J. Comput. Phys.* 218 (1) (2006) 19–43.
- [9] D.W. Boyer, An experimental study of the explosion generated by a pressurized sphere, *J. Fluid Mech.* 9 (1960) 401–429.
- [10] H.L. Brode, *Theoretical Solutions of Spherical Shock Tube Blasts*, The RAND Corporation, RM-1974, 1957.
- [11] R. Courant, K.O. Friedrichs, *Supersonic Flow and Shock Waves*, Interscience, New York, 1948.
- [12] J. Falcovitz, A. Birman, A singularities tracking conservation laws scheme for compressible duct flows, *J. Comput. Phys.* 115 (2) (1994) 431–439.
- [13] M.P. Friedman, A simplified analysis of spherical and cylindrical blast waves, *J. Fluid Mech.* 11 (1961) 1–15.
- [14] I.I. Glass, *Nonstationary Flows and Shock Waves*, Oxford Science Publications, Oxford, 1994.
- [15] E. Godlewski, P.-A. Raviart, Numerical approximation of hyperbolic systems of conservation laws, *Applied Mathematical Sciences*, vol. 118, Springer, 1996.
- [16] S.K. Godunov, A finite difference method for the numerical computation and discontinuous solutions of the equations of fluid dynamics, *Mat. Sb.* 47 (1959) 271–295.
- [17] L. Krivodonova, M. Berger, High-order accurate implementation of solid wall boundary conditions in curved geometries, *J. Comput. Phys.* 211 (2006) 492–512.
- [18] A. Lapidus, Computation of radially symmetric shocked flows, *J. Comput. Phys.* 8 (1971) 106–118.
- [19] Ph. LeFloch, P.-A. Raviart, An asymptotic expansion for the solution of the generalized Riemann problem I General theory, *Ann. Inst. H. Poincaré é Anal. Non Linéaire* 5 (2) (1988) 179–207.
- [20] J. Li, G. Chen, The generalized Riemann problem method for the shallow water equations with bottom topography, *Int. J. Numer. Meth. Eng.* 65 (6) (2006) 834–862.
- [21] J. Li, Z. Sun, Remark on the generalized Riemann problem method for compressible fluid flows, *J. Comput. Phys.* 222 (2) (2007) 796–808.
- [22] R. Liu, *The Computation of Spherical Compressible Fluid Flows by the GRP Scheme*, Master Thesis, Capital Normal University, 2006.
- [23] T.G. Liu, B.C. Khoo, K.S. Yeo, The numerical simulations of explosion and implosion in air: use of a modified Harten's TVD scheme, *Int. J. Numer. Meth. Fluids* 31 (1999) 661–680.
- [24] P. Maire, B. Nkonga, Multi-scale Godunov-type method for cell-centered discrete Lagrangian hydrodynamics, *J. Comput. Phys.* 228 (3) (2009) 799–821.
- [25] W.F. Noh, Errors for calculations of strong shocks using an artificial viscosity and artificial heat flux, *J. Comput. Phys.* 72 (1987) 78–120.
- [26] M. Omang, S. Børve, J. Trulsen, SPH in spherical and cylindrical coordinates, *J. Comput. Phys.* 213 (2006) 391–412.
- [27] A.Y. Poludnenko, A.M. Khokhlov, Computation of fluid flows in non-inertial contracting expanding and rotating reference frames, *J. Comput. Phys.* 220 (2007) 678–711.
- [28] P.L. Sachdev, *Shock waves and explosions*, Pitman Monographs and Surveys in Pure and Applied Mathematics, vol. 132, Chapman and Hall/CRC, 2004.
- [29] L.I. Sedov, *Similarity and Dimensional Methods in Mechanics*, Academic Press, New York, 1959.
- [30] G.A. Sod, A numerical study of a converging cylindrical shock, *J. Fluid Mech.* 83 (1977) 785–794.
- [31] G.A. Sod, A survey of several finite difference methods for systems of nonlinear hyperbolic conservation laws, *J. Comput. Phys.* 27 (1978) 1–31.
- [32] E.F. Toro, *Riemann Solvers and Numerical Methods for Fluid Dynamics: A Practical Introduction*, Springer, 1997.